ARC Geophysical Research

The Bathymetric Effect and Epilimnetic Turbidity in a Glacier-Fed Hydroelectric Reservoir

Daniel M. Robb*[1], Roger Pieters[1,2], and Gregory A. Lawrence[1]

[1]Department of Civil Engineering, University of British Columbia, Vancouver, BC, Canada
[2]Department of Earth, Ocean and Atmospheric Sciences, University of British Columbia, Vancouver, BC, Canada

Abstract

Turbidity limits light availability in many glacier-fed lakes and reservoirs, with far-reaching ecological consequences. We use field observations and hydrodynamic modelling in conjunction with 46 years of hydrological data to examine the physical processes affecting turbidity in the epilimnion (surface layer) of glacier-fed Carpenter Reservoir, British Columbia, Canada. We analyze responses to changes in reservoir operations (e.g. water level, inflows and withdrawals), and to natural processes (e.g. particle settling, internal seiching and wind-driven upwelling). The combination of cold inflows and deep outlets leads to plunging inflows and the isolation of the epilimnion. This isolation, along with particle settling, results in a remarkable clearing of the epilimnion during summer.

As the reservoir fills in spring, there is a net inflow to the hypolimnion (lower layer), which displaces the epilimnion upwards and causes the epilimnion to thin as it spreads over an increased area. As the epilimnion thins, it becomes progressively more vulnerable to wind events until a wind event occurs that is strong enough to upwell water from the metalimnion (the intermediate layer between the epilimnion and the hypolimnion) into the epilimnion, thereby increasing the thickness of the epilimnion. If the wind stops and the inflow persists, the epilimnion will begin to thin again until the next significant wind event. This process, known as the bathymetric effect, typically repeats itself several times during spring freshet and provides an indirect path for the transport of high turbidity inflows into the epilimnion of Carpenter Reservoir. We introduce the bathymetric inflow parameter, I_B, representing the balance between particle settling from the epilimnion and the upward transport of turbid water into the epilimnion. We find that I_B during spring controls epilimnetic turbidity at the beginning of summer, which, in turn, is the primary determinant of turbidity and light penetration for the rest of the summer.

Keywords: Physical Limnology, Turbidity, Glacial Inflow, Bathymetric Effect

*Corresponding Author
E-mail addresses: drobb@eoas.ubc.ca, rpieters@eoas.ubc.ca, lawrence@civil.ubc.ca

1 Introduction

Through the construction and operation of an estimated 500,000 reservoirs greater than one hectare [7], humans have dramatically altered the hydrology, particle fluxes and biogeochemistry of freshwater ecosystems on a global scale [11, 20, 38]. Worldwide, 48% of river volume is moderately to severely impacted by dams, and with dams currently planned or under construction this fraction would increase to 93% [13]. With an increasing proportion of the world's freshwater affected by dams, understanding the environmental response to changes in reservoir operations and hydrological conditions is critical to sustaining freshwater ecosystems [25].

Dammed reservoirs provide 30% of the world's irrigation water [40] and 17% of global electricity generation through hydropower [26], as well as drinking water, flood control and navigation routes. Despite these benefits, there is a heightened awareness of their ecological and water quality impacts [39]. Various of these impacts have been studied, including the pathway of nutrients from plunging inflow to the euphotic zone [10, 24, 31]; changes in downstream nutrients [1], turbidity [9] and light [15]; and the effects on biological productivity of converting a lake into a reservoir [21].

In the present study we focus on turbidity, which is an important indicator of water quality, notably in glaciated catchments where high turbidity from glacial meltwater is often the dominant factor reducing the penetration of light into the water column [30], thereby impacting primary productivity [32], plankton community composition [34], filter-feeding organisms [19] and predator-prey dynamics [16].

We consider Carpenter Reservoir, a hydroelectric reservoir in southwest British Columbia, Canada (Figure 1a). Carpenter Reservoir supports populations of kokanee (*Oncorhynchus nerka*), a landlocked sockeye salmon, as well as sport fish such as rainbow trout (*Oncorhynchus mykiss*) and bull trout (*Salvelinus confluentus*), see Hirst [14]. The province of British Columbia's hydroelectric utility (BC Hydro) is concerned that turbidity is limiting light penetration, reducing algal growth, and decreasing fisheries productivity within Carpenter Reservoir. This concern prompted an extensive field study of the physical limnology of Carpenter Reservoir during 2015 and 2016 [29].

Robb et al. [29] observed elevated turbidity throughout Carpenter Reservoir during spring turnover. However, once the reservoir stratified, thermal stratification isolated the epilimnion (surface layer) from the cold and turbid inflows that plunged into the hypolimnion (lower layer). Meanwhile, glacial fines settled out of the epilimnion and by the end of summer, measured epilimnetic turbidities were more than an order of magnitude lower than those in the hypolimnion. There was also a longitudinal decrease in epilimnetic turbidity along the length of the reservoir. Applying a one-dimensional (longitudinal) diffusion equation to the field measurements, Robb et al. [29] were able to estimate the settling velocity ($\approx 0.25\ \mathrm{m\,d^{-1}}$), the longitudinal dispersion coefficient ($50 - 70\ \mathrm{m^2\,s^{-1}}$), and the flux of turbid water into the epilimnion ($\approx 1\%$ of the total inflow into the reservoir). The first two estimates agree favourably with published data. However, the limited turbidity data — both spatially and temporally — prevented an assessment of the processes governing the intermittent flux of turbidity into the epilimnion and the fluctuations of turbidity on time scales less than a month. In the present study we use a two-dimensional hydrodynamic model, which allows us to examine the processes governing epilimnetic turbidity at much finer spatial and temporal resolution.

doi: https://doi.org/10.5149/ARC-GR.1365

While the results of Robb et al. [29] suggest that epilimnetic turbidity in Carpenter Reservoir might not be a concern, questions still remain. Were 2015 and 2016 representative years? Are higher epilimnetic turbidities possible? And, if so, under what circumstances? Like most other hydroelectric reservoirs in temperate latitudes, Carpenter Reservoir is typically drawn down in winter for electricity generation and allowed to fill again during spring freshet. When the spring freshet plunges into the hypolimnion, the epilimnion is displaced upwards and thins as it spreads over a larger area. The epilimnion is then more susceptible to wind-driven upwelling and surface mixed layer deepening. This, so called bathymetric effect [24], provides an indirect path for the transport of high turbidity inflow into the epilimnion.

The bathymetric effect may have been less important in 2015 and 2016 since Carpenter Reservoir was not drawn down particularly low in those years, see Figure 1c in Robb et al. [29]. However, in many other years the reservoir was drawn down much lower in winter, and we hypothesize that the bathymetric effect may have been important. In the present paper, we investigate this hypothesis numerically using 46 years of water level, inflow and outflow measurements collected by BC Hydro, in conjunction with the meteorological and limnological data collected in 2015. We also investigate how particle settling, wind-driven upwelling, internal seiching, longitudinal dispersion, and convective cooling act together with the bathymetric effect to determine epilimnetic turbidity.

In Section 2 we provide background information on Carpenter Reservoir, analyze the potential implications of the bathymetric effect and introduce the bathymetric inflow parameter. Section 3 describes the hydrodynamic model. Section 4 presents the model results obtained using 46 years of measured inflow, outflow and water level data, in conjunction with the limnological and meteorological data collected in 2015. We discuss the results in Section 5 and present a summary of the paper in Section 6.

2 Background

2.1 Study Site

Carpenter Reservoir ($50°51'$ N, $122°30'$ W) is part of the Bridge River hydroelectric complex, located $\sim$200 km north of Vancouver, British Columbia, Canada (Figure 1a). Carpenter Reservoir, formed by the construction of Terzaghi Dam in 1960, is long ($\sim$50 km) and narrow ($\sim$1 km), with a maximum surface area of 46 km^2 and a maximum depth of 50 m (Figure 1b). Inflows into the reservoir contain high concentrations of fine glacial particles, which are slow to settle and give the water a characteristic cloudy (turbid) appearance.

The primary source of glacial meltwater and fine particles into Carpenter Reservoir is the Bridge Glacier, which forms the headwaters of the Upper Bridge River. Water from the Upper Bridge River flows into Downton Reservoir created by La Joie Dam (Figure 1a). The cold and turbid water discharged from La Joie Dam into the Middle Bridge River is the single largest inflow into Carpenter Reservoir. When Carpenter Reservoir is below full pool, this inflow runs along the original riverbed through the draw-down zone until reaching the reservoir (Figure 1c), unlike when the reservoir is full (Figure 1d). The balance of the inflow, referred to as the local inflow, includes major tributaries such as the Hurley River, Gun Creek and Tyaughton Creek (Figure 1a), along with inflow from the rest of the drainage through tributaries of all sizes, as well as precipitation to, and evaporation from, the lake surface.

The vast majority of the water in Carpenter Reservoir is diverted through twin tunnels to Seton Lake (Figure 1a), with an elevation drop of $\sim$400 m used for generating hydroelectricity. A small amount of water is released through low-level outlets at Terzaghi Dam to the Lower Bridge River to maintain a minimum environmental flow. Note, all the outlets are from the deepest part of the reservoir. The diversion of water from Carpenter Reservoir to Seton Lake

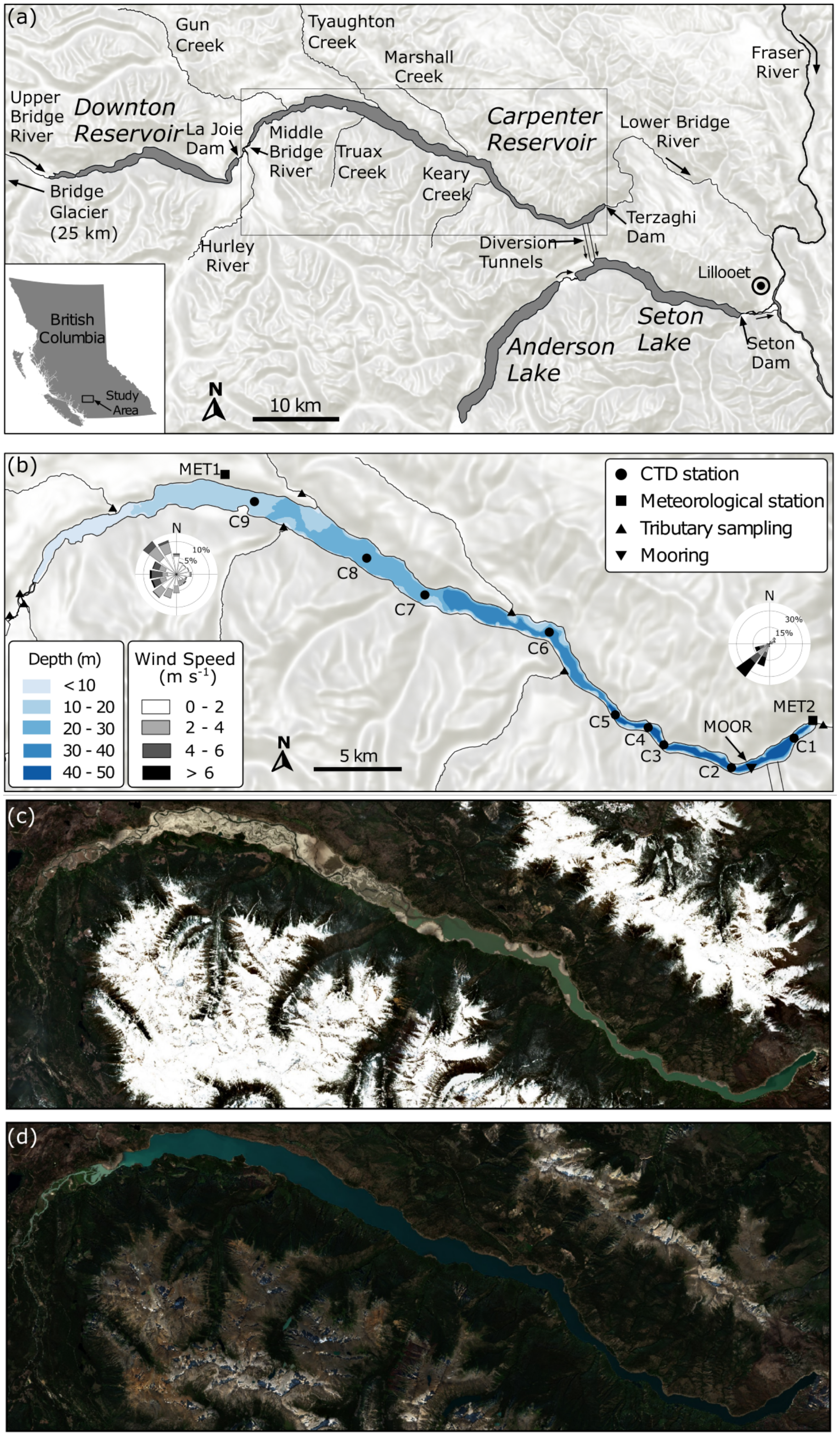

Figure 1: (a) Map of the study area. The box marks the location of panel (b). The Bridge Glacier is located 25 km upstream of the map boundary. (b) Plan view of Carpenter Reservoir and monitoring stations. The contours indicate the depth of water below full pool (651.08 m asl). Wind roses are shown for Five Mile Station (MET1) and Terzaghi Dam (MET2). Major tributaries flowing into Carpenter Reservoir are shown as solid lines. Sentinel-2 satellite images showing Carpenter Reservoir at (c) low water level on 9 May 2024 and (d) high water level on 1 September 2024.

is the main component of the Bridge River hydroelectric complex, which is British Columbia's third largest, with a maximum generating capacity of 492 MW, accounting for 6 − 8% of the province's electrical supply [3]. As a result, changes in reservoir operations have important economic consequences.

2.2 Historical Data

Daily inflow, outflow and water level data for Carpenter Reservoir were provided by BC Hydro for the period 1961 to 2017. The inflow data consisted of the regulated discharge released from La Joie Dam, which flows into the Middle Bridge River and then into Carpenter Reservoir (Figure 1a). The outflow data included the deep withdrawals from Carpenter Reservoir to Seton Lake and the Lower Bridge River. The local inflow, Q_{loc}, into Carpenter Reservoir was computed from a water balance using the outflows to Seton Lake, Q_{sl}, and the Lower Bridge River, Q_{lbr}; the inflow from La Joie Dam, Q_{laj}; along with the change in reservoir volume $\frac{\mathrm{d}V}{\mathrm{d}t}$:

$$Q_{\mathrm{loc}} = Q_{\mathrm{sl}} + Q_{\mathrm{lbr}} - Q_{\mathrm{laj}} + \frac{\mathrm{d}V}{\mathrm{d}t} \,. \tag{1}$$

Data of sufficient quality and completeness for the application of the hydrodynamic model were available for the period 1965 to 2017, excluding seven years with significant spill from Terzaghi Dam (1972, 1974, 1976, 1982, 1983, 1984 and 1991), for a total of 46 years.

2.3 Field Methods

During the biologically productive season (May to October) of 2015 and 2016, measurements were collected of the physical limnology of Carpenter Reservoir [29]. Monthly CTD (conductivity, temperature, depth) profiles were collected at up to nine locations along the reservoir (Figure 1b) using a Sea-Bird SBE 19plus V2 (accuracy ±0.005 °C, ±1 $\mu\mathrm{S\,cm^{-1}}$) profiler equipped with a WETLabs ECO combined fluorometer and optical backscatter (turbidity) sensor, a Biospherical photosynthetically active radiation (PAR) sensor, and a SBE 43 dissolved oxygen sensor. Data from the downcasts are shown; samples were collected at 4 Hz with a descent rate of $\sim 0.2\ \mathrm{m\,s^{-1}}$, giving a vertical resolution of 5 cm.

To characterize the inflow, we sampled water temperature, conductivity and turbidity in the outflow of La Joie Dam and in six tributaries: Hurley, Gun, Truax, Tyaughton, Marshall, and Keary (Figure 1a). These six tributaries drain 83% of the local watershed. The outflow from La Joie Dam and the six tributaries were sampled monthly using a YSI multi-parameter probe, and continuous measurements of water temperature were recorded at 20-min intervals using Onset Hobo TidbiT v2 temperature loggers (UTBI-001, accuracy ±0.25 °C).

In addition, continuous measurements of water temperature were recorded from temperature loggers attached to a mooring suspended from a log boom near the deepest part of the reservoir (Figure 1b). The loggers were mostly the Onset Hobo Water Temperature Pro v2 (U22-001, accuracy ±0.2 °C, 20-min intervals) as well as several of the RBR Solo T (accuracy ±0.002 °C, 10-s intervals) at selected depths. Meteorological data were collected at two onshore stations along the reservoir (Figure 1b).

Measurements made using an Elzone 280 Coulter counter showed that the suspended particles in Carpenter Reservoir were predominately clay sized ($< 2\ \mu$m). The contributions of turbidity and conductivity to density were negligible, and density differences in Carpenter Reservoir were controlled by temperature [29].

2.4 Field Data

Field data from 2015 were used to drive the hydrodynamic model. In 2015, the local inflow peaked during spring freshet and declined into the summer (Figure 2a). In contrast, the inflow

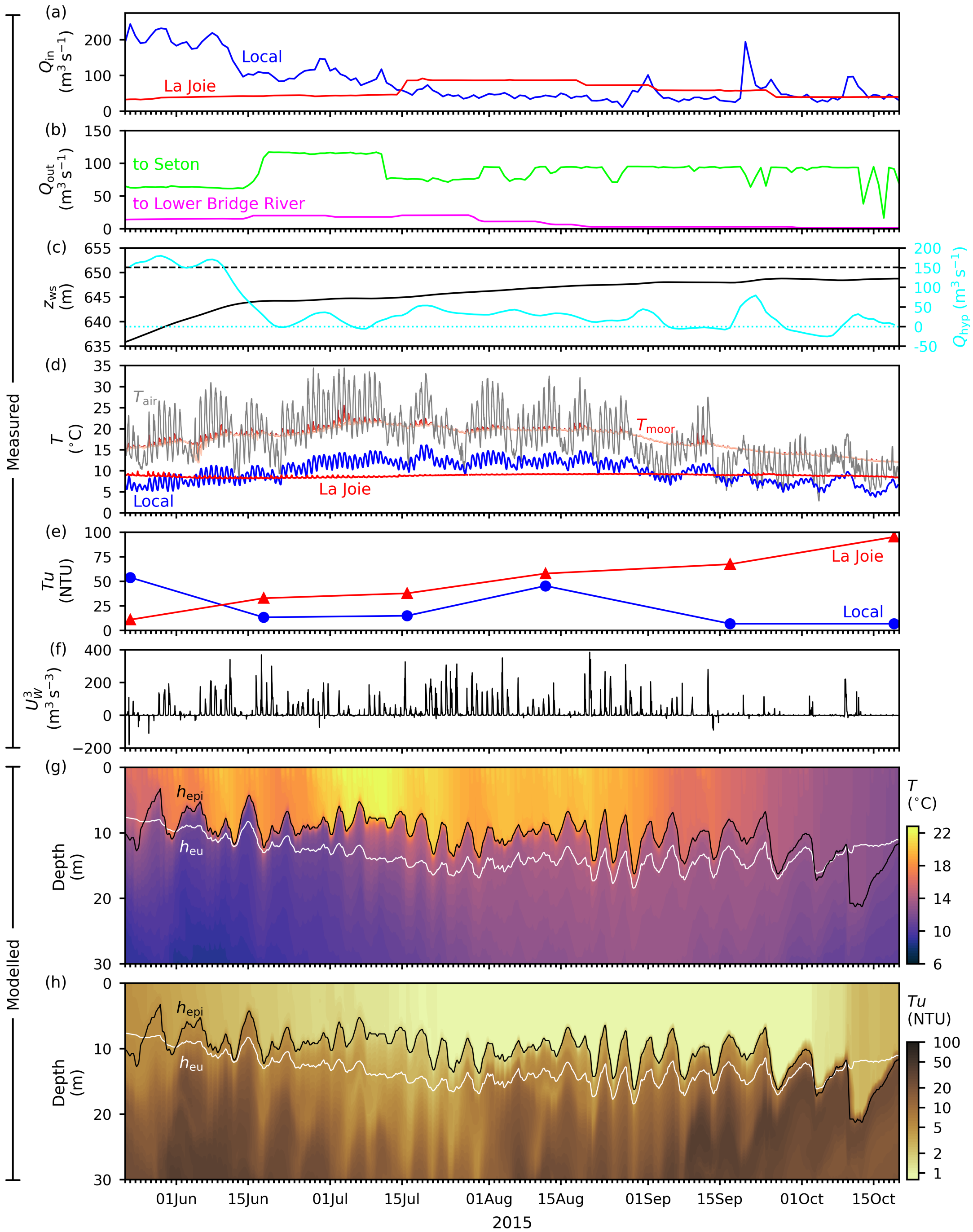

Figure 2: Measured (a) inflows, (b) outflows, (c) water level, (d–e) flow-weighted tributary temperature and turbidity, (f) along-axis wind speed cubed; and modelled (g–h) temperature and turbidity at Station C2, 22 May to 20 October 2015. In (c), the dashed line marks full pool (651.08 m asl). In (d), air temperature and mooring temperature (0–5 m below the water surface) are shown in grey and shades of red, respectively. In (f), positive wind is from the west toward the dam. In (g–h), the black line marks the epilimnion depth (maximum temperature gradient) and the white line the euphotic depth [28, Equation 4.3]. In (a,d,e), "La Joie" marks the regulated inflow released from La Joie Dam and "Local" marks the unregulated inflow from the local tributaries. The local inflow in (a) and Q_{hyp} in (c) are calculated from observed quantities). In (h), the colour scale is logarithmic.

from La Joie Dam was relatively constant, except for steps when electrical generation was altered (Figure 2a). Outflow to Seton Lake was generally steady, and the outflow through Terzaghi Dam to the Lower Bridge River was low (Figure 2b). The water level variation in 2015 was typical for a hydroelectric reservoir in Canada, low in April and filling during freshet (Figure 2c).

From May to October 2015, the temperature of the inflow from La Joie Dam was relatively steady, between 8 and 10 °C (Figure 2d, red). By contrast, the temperature of the local inflow showed strong seasonal and diurnal variations (Figure 2d, blue). Both the inflow from La Joie Dam and from the local inflow were cooler than the epilimnion (Figure 2d, shades of red). Inflow from La Joie Dam (catchment 19% glaciated) was generally more turbid than inflow from the local tributaries (catchment $< 2\%$ glaciated), see Figure 2e. Note the high turbidity of the local inflow on 23 May 2015 may have bias, as samples were collected after a rainstorm the previous evening. In May and June, plunging inflow to the hypolimnion was dominated by local tributaries with high turbidity (Figure 2e). In late summer and early fall, inflow from La Joie Dam dominated with a turbidity that rose steadily to nearly 100 NTU by October 2015 (Figure 2e).

Carpenter Reservoir is located in a steep mountain valley, with some slopes gaining more than 2000 m from the water surface in less than 10 km. The available data indicate that the wind over Carpenter Reservoir is channelized and generally follows the reservoir as the orientation of the valley changes (Figure 1b, insets). From May to October, the prevailing winds were down-valley toward Terzaghi Dam (Figure 2f, $U_W^3 > 0$); up-valley winds were infrequent and weak (Figure 2f, $U_W^3 < 0$). The wind showed a strong diurnal pattern, rising in late morning, peaking in the afternoon, and declining to $< 1\ \mathrm{m\,s^{-1}}$ in the evening (Figure 2f).

2.5 Bathymetric Effect

Here we investigate the importance of the bathymetric effect [24] in the context of Carpenter Reservoir. Consider an idealized, stratified reservoir into which all inflows, Q_{in}, plunge into the hypolimnion and all outflows, Q_{out}, are withdrawn from the hypolimnion, as depicted in Figure 3a. This serves as a useful idealization for many hydroelectric reservoirs in temperate latitudes, including Carpenter Reservoir, that are typically drawn down in winter for electricity generation and allowed to fill again during spring freshet. During spring freshet the net hypolimnetic inflow rate, $Q_{\mathrm{hyp}} = Q_{\mathrm{in}} - Q_{\mathrm{out}}$, is almost always positive, and as the reservoir fills the epilimnion is displaced upwards and thins as it spreads over a larger area (Figure 3b). As the epilimnion thins, it becomes progressively more vulnerable to wind events until a wind event occurs that is strong enough to mix hypolimnetic water into the epilimnion, thereby increasing its thickness, see Section 2.6 below. If the wind stops and the inflow persists, the epilimnion will begin to thin again until the next significant wind event. This process, known as the bathymetric effect, typically repeats itself several times throughout spring freshet, and provides an indirect path for the transport of high turbidity inflows into the epilimnion of Carpenter Reservoir.

To analyze the bathymetric effect, consider the pycnocline (zone of high vertical density gradient), which in our idealized two-layer model is the interface between the epilimnion and hypolimnion (Figure 3). For Carpenter Reservoir, where density is controlled by temperature, the pycnocline is effectively the same as the thermocline (zone of high vertical temperature gradient). The rate of change of the pycnocline elevation:

$$\frac{\mathrm{d}z_{\mathrm{pyc}}}{\mathrm{d}t} = \frac{Q_{\mathrm{hyp}}}{A_{\mathrm{pyc}}}\,, \tag{2}$$

where z_{pyc} is the pycnocline elevation and A_{pyc} is the surface area of the pycnocline. Similarly,

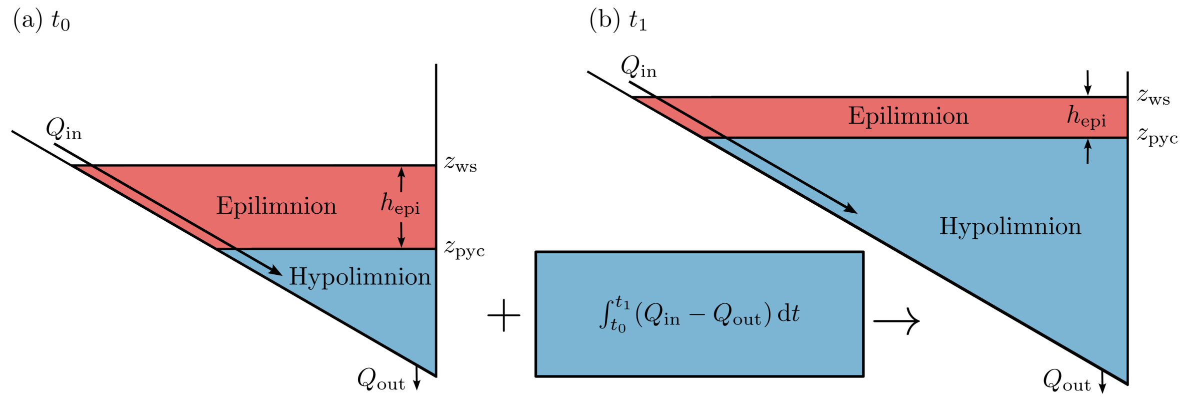

Figure 3: Schematic showing a reservoir (a) before and (b) after inflow from spring freshet. The inflow is denser than the epilimnion and plunges into the hypolimnion. As the water level rises, the epilimnion becomes longer and thinner, and more susceptible to wind-driven mixing. The water levels in panels (a) and (b) are representative of Carpenter Reservoir on 28 May and 20 June 2017, respectively.

consider the rate of change of water surface elevation:

$$\frac{\mathrm{d}z_{\text{ws}}}{\mathrm{d}t} = \frac{Q_{\text{hyp}}}{A_{\text{ws}}} , \tag{3}$$

where z_{ws} is the water surface elevation and A_{ws} is the water surface area. Subtracting (2) from (3) yields:

$$\frac{\mathrm{d}h_{\text{epi}}}{\mathrm{d}t} = -\frac{\beta Q_{\text{hyp}}}{A_{\text{pyc}}} , \tag{4}$$

where $h_{\text{epi}} = z_{\text{ws}} - z_{\text{pyc}}$ is the thickness of the epilimnion, and $\beta = (1 - A_{\text{pyc}}/A_{\text{ws}})$ is the bathymetric factor [24]. The variation of the bathymetric factor as a function of the water surface level in Carpenter Reservoir is plotted in Figure 4a. Note, the flattening of the curve as the water level reaches an elevation of 620 to 630 m results from the substantial widening of the reservoir. Using (4) we define a retention time for the epilimnion:

$$\tau_B \equiv \frac{h_{\text{epi}}}{\left|\frac{\mathrm{d}h_{\text{epi}}}{\mathrm{d}t}\right|} = \frac{A_{\text{pyc}} h_{\text{epi}}}{\beta Q_{\text{hyp}}} . \tag{5}$$

We can compare τ_B with the timescale for particle settling out of the epilimnion,

$$\tau_s \equiv \frac{h_{\text{epi}}}{w_s} , \tag{6}$$

where w_s is the settling velocity. Following the approach used by Robb et al. [29], we obtain the bathymetric inflow parameter:

$$I_B \equiv \frac{\tau_s}{\tau_B} = \frac{\beta Q_{\text{hyp}}}{A_{\text{pyc}} w_s} . \tag{7}$$

We anticipate that I_B is an important indicator of changes in epilimnetic turbidity due to the bathymetric effect. When I_B is small, settling dominates, and when I_B is large, the bathymetric effect dominates. In Carpenter Reservoir, the ratio β/A_{pyc} is sensitive to changes in water level, particularly at low water levels (Figure 4b). Note, that in real systems, the hypolimnetic inflow, Q_{hyp}, is time varying (Figure 6c), as is β/A_{pyc} (Figure 6d), and,

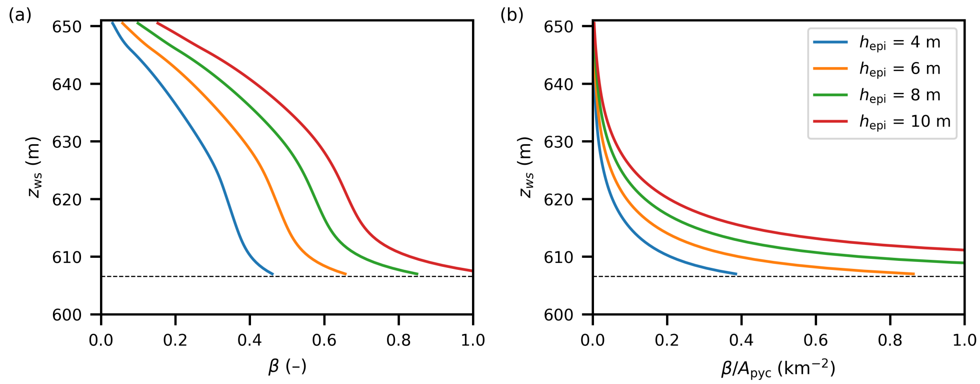

Figure 4: (a) The bathymetric factor, β, and (b) the ratio of the bathymetric factor divided by the surface area of the pycnocline, β/A_{pyc}, as a function of water surface elevation for h_{epi} = 4, 6, 8, 10 m. The dashed line marks the minimum operating water level (606.55 m asl).

consequently, I_B can be highly variable. To assess the importance of the bathymetric effect, it is appropriate to time average I_B over a long enough period to include at least one cycle of epilimnetic thinning (due to hypolimnetic inflow), followed by epilimnetic thickening (due to wind mixing). In the present study we focus on spring 2015, during which there were three such cycles in a period of 30 days (Figure 2f). Other factors causing fluctuations in epilimnetic turbidity, including the passage of internal waves and wind-driven advection along the length of the reservoir, will be discussed in Sections 4 and 5.

2.6 Response of a Lake to Wind

The response of a lake or reservoir to wind is a crucial factor in determining its physical limnology, including, in the case examined here, the temporal and spatial variation of epilimnetic turbidity. In the two-layer idealization presented in Figure 3, wind exerting a shear stress on the water surface results in a downward tilting of the interface between the epilimnion and the hypolimnion. Changes in the wind generate internal waves, known as "internal seiches", on the interface [5, 23]. The phase speed, c_p, and period, T_1, of the fundamental (basin scale) internal seiche can be approximated by the Merian formulae:

$$c_p = \sqrt{g' \frac{h_{\mathrm{epi}}\, h_{\mathrm{hyp}}}{h_{\mathrm{epi}} + h_{\mathrm{hyp}}}} \qquad \text{and} \qquad T_1 = \frac{2L}{c_p} \,, \tag{8}$$

where $g' = g\,(\rho_{\mathrm{hyp}} - \rho_{\mathrm{epi}})\,/\rho_{\mathrm{hyp}}$ is the reduced gravitational acceleration, and ρ_{epi} and ρ_{hyp} are the densities of the epilimnion and hypolimnion, respectively. We take h_{epi} and h_{hyp} as the volume-weighted average depth of the epilimnion and hypolimnion, respectively; and L as the length of the lake in the wind direction at the undisturbed elevation of the interface.

The effect of wind forcing on basin-scale internal motions is characterized by the Wedderburn number [37]:

$$W = \frac{g' h_{\mathrm{epi}}^2}{u_*^2 L} \,, \tag{9}$$

where $u_* = U_W \sqrt{C_D \rho_A / \rho_{\mathrm{epi}}}$ is the shear velocity, U_W is the wind speed measured at a height of 10 m and averaged over $T_1/4$, $C_D \approx 1.3 \times 10^{-3}$ is the drag coefficient, and $\rho_A \approx 1.2\ \mathrm{kg\,m^{-3}}$ is the density of air. The Wedderburn number is a measure of the ratio of the epilimnetic

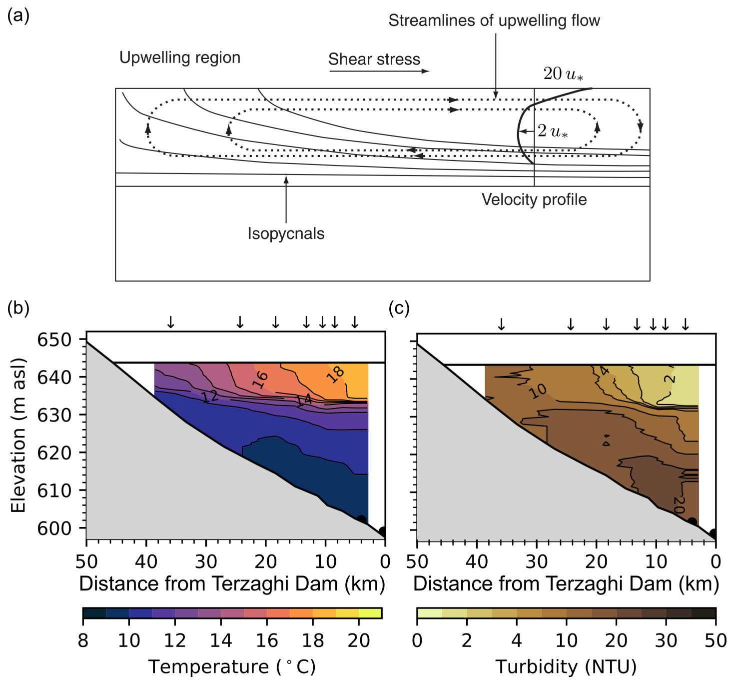

Figure 5: Wind-driven upwelling. (a) Schematic adapted from Monismith [22, Figure 22] and contours of (b) temperature and (c) turbidity from field measurements in Carpenter Reservoir on 18 June 2015 when $W = 1.1$, adapted from Robb et al. [29, Figure 6]. In (b,c), the downward arrows mark the location of the CTD profiles.

thickness to the internal seiche amplitude, and the response of a lake to wind is strongly linked to the value of the Wedderburn number:

(i) When $W \gg 1$, the internal seiches are relatively small, and once the wind stops, they will dampen out, resulting in minimal mixing between the two layers.

(ii) When $W = O(1)$, the response of the lake is more complicated, but the most relevant to the present study. In this case, it is important to recognize that in real lakes there is an intermediate layer of finite thickness, called the metalimnion, between the epilimnion and hypolimnion. Across the metalimnion the temperature and density typically vary smoothly between those of the epilimnion and hypolimnion. In Carpenter Reservoir, turbidity also varies smoothly across the metalimnion. As the wind blows, the isopycnals remain almost horizontal at the base of the metalimnion, but slope upward more and more dramatically towards the top of the metalimnion. This process, known as wind-driven upwelling, affects the water column from the water surface down to the base of the metalimnion and has been observed in the laboratory (e.g. Monismith [22]) and in many lakes and reservoirs, including Carpenter Reservoir, see Figure 5. A proportion of the metalimnion upwells to the surface at the upwind end of the reservoir, and this proportion increases as the Wedderburn number decreases. The upwelled fluid, containing turbid fluid that originated in the hypolimnion in the case of Carpenter Reservoir, is transported downstream by wind-driven surface currents and mixes with epilimnetic fluid in the process. When the wind stops, upwelling ceases and the isopycnals return to horizontal. The final result is a deeper and, in the case of Carpenter Reservoir, a more turbid epilimnion than before the wind event.

(iii) When $W \ll 1$, strong upwelling occurs that can result in complete mixing of the lake if the wind persists for long enough. This case is not relevant to the present study.

2.7 Particle Settling

To estimate the rate of particle settling from the epilimnion, we apply the approach of Smith [33], Reynolds [27] and Tedford et al. [36], which describes the exponential decline of epilimnetic turbidity:

$$Tu_f = Tu_i \exp\left(-\frac{t_f - t_i}{\tau_s}\right), \tag{10}$$

where the subscripts i and f denote the initial and final times, respectively. The characteristic timescale, $\tau_s = h_{\mathrm{epi}}/w_s$, represents the time required for epilimnetic turbidity to decrease by a factor of $1/e$ in the absence of the bathymetric effect and additional mixing processes such as wind-driven turbulence or convective cooling. When these mixing processes are present, turbidity may decline at a reduced *effective* settling velocity, w_s^{eff}, compared to the velocity of particle settling, w_s, in quiescent conditions.

3 Hydrodynamic Model

To understand the physical processes influencing turbidity in Carpenter Reservoir, simulations were conducted using the two-dimensional laterally averaged hydrodynamic and water quality model, CE-QUAL-W2 version 3.72 [6]. This model captures the dynamics along the length of the reservoir while ensuring that the run time is modest, making it possible to explore a wide range of scenarios. As the focus of the present study is on the bathymetric effect, we provide a brief description of the model here and refer the interested reader to Robb [28] for full details.

The model domain extends from the upstream end of Carpenter Reservoir to Terzaghi Dam (Figure 1a). Model runs were initialized with the measured water temperature, turbidity and conductivity from the May CTD profile at Station C2 (Figure 1b). The profile was vertically aligned with the initial water level of each model year. That is, if the initial water level was shallower than in 2015, the initial profile was cut off at the bottom to match the initial water depth of the given year. If the initial water level was deeper than in 2015, the initial profile was extended using the deepest value in the 2015 profile.

The model was set up with inflows from La Joie Dam and the local drainage, and outflows to Seton Lake and the Lower Bridge River (Figure 1a). We divided the local inflow into thirteen sub-catchments based on watershed topography and the various reaches in the reservoir. The local inflow was then distributed among the thirteen sub-catchments in proportion to their drainage areas. For six of the thirteen sub-catchments, we assumed water properties to be that of the tributary sampled in that sub-catchment. For the remaining seven sub-catchments, where no direct sampling was conducted, we assumed tributary water properties similar to those of Keary Creek, as it represents a reasonable proxy based on its drainage characteristics. Flow-weighted averages for the properties, S, of the local inflow were calculated as $\langle S\rangle = \sum Q_i S_i / \sum Q_i$, where Q_i is the flow rate of sub-catchment i, and $i = 1$ to 13.

In the model, tributary inflows were represented by thirteen point-discharges to the nearest horizontal segment and placed into the water column at the depth of neutral buoyancy, which, of the options provided in the model, was most appropriate. The inflow water temperature, turbidity and conductivity were linearly interpolated between measurements to the model time step. We assume groundwater inflows and outflows are negligible. The density of water was computed using the model's default equation of state, which accounts for density variations due to changes in water temperature, suspended solids and dissolved solids [6, p. A-125].

Meteorological boundary conditions were driven by wind data from Five Mile Station located along the main fetch (MET1), and solar radiation, air temperature and relative humidity data collected on Terzaghi Dam (MET2, Figure 1b). Simulations began on the date of the first sampling trip and ended on the date of the last sampling trip: 22 May 2015 to 20 October 2015.

The model was calibrated by adjusting a small subset of parameters until the computed results best matched the field observations [28, Table A.1]. The first step was a comparison of the measured and modelled water temperature, followed by conductivity, and finally turbidity. The root mean square error (RMSE) between the modelled temperature, conductivity and turbidity and the CTD measurements for 2015 was 0.80 °C, 9.1 $\mu S\,cm^{-1}$, and 5.7 NTU, respectively (with RMSE for turbidity in the epilimnion of 1.7 NTU), while the RMSE between the modelled and moored temperature was 0.88 °C [28, Table A.2 and Figures A.1–A.7]. This agreement is comparable to that reported in similar model studies [12, 18, 35].

The model results for 2015 illustrate the seasonal evolution of the thermocline as the epilimnion warmed in summer and then cooled and deepened in fall (Figure 2g). There were times when the depth of the modelled thermocline oscillated over periods of 4 to 5 days due to wind-driven internal seiching. For example, the prevailing wind from the west pushed the warm epilimnion toward Terzaghi Dam, deepening the epilimnion near the dam (15 July 2015, Figure 2f,g), and when the wind subsided, the epilimnion near the dam became shallower again (17 July 2015, Figure 2f,g). From 22 May to 5 September 2015, the simulated turbidity of the epilimnion declined from 5.2 to 0.5 NTU, whereas turbidity in the deep water was much higher, dominated by local tributary inflow which plunged to depth (Figure 2h).

Following the model calibration [28, Appendix A], the model was run using the 46 years of historical inflows and operational conditions, see Section 2.2. Over the life of the reservoir, it has been operated in a variety of ways in response to hydrological conditions (e.g. wet and dry years), variations in electricity demand, changes in ecological constraints, and operational considerations (e.g. maintenance). To represent this variability, we ran the model driven by the inflows and outflows for each of the 46 years. These flows, along with the water level at the start of the model run, reproduced the water level for a given year. However, meteorological, CTD, and tributary sampling (temperature, conductivity and turbidity) data needed for the initial and boundary conditions (referred to hereafter as meteorological and limnological forcing), were only available for 2015 and 2016. Model results using the meteorological and limnological forcing from 2015 are presented in the present paper, while the model results using the corresponding forcing from 2016 are presented in Robb [28]. For the remainder of this paper, we will use the term “the [year] model run” for the simulation using the flow and water level forcing from [year] and the meteorological and limnological forcing from 2015.

Since meteorological and limnological forcing were not available for each of the 46 years, the model runs do not represent the water quality conditions during those years; rather, they represent a synthetic dataset generated using 46 years of measured flows subject to the meteorological and limnological boundary conditions collected in 2015. Subjecting various operational conditions to the same set of meteorological and limnological forcing provided a basis for comparison between scenarios by removing the effects of interannual variability in the meteorological and limnological data, thereby focusing on the importance of the bathymetric effect.

4 Modelled Scenarios Driven by Historical Flows (1965 – 2017)

Here we examine scenarios of epilimnetic turbidity variation in Carpenter Reservoir obtained by simulating the reservoir hydrodynamics using the inflows and outflows from 1965 to 2017, in conjunction with the meteorological and limnological data collected in 2015. The turbidity of the epilimnion for each of these simulations at station C2 are shown in Figure 6f. While the epilimnetic turbidity can vary by up to an order of magnitude between scenarios, the seasonal variations follow relatively well-defined patterns. Spring is characterized by calm periods where settling dominates (Regime I), resulting in gradual declines in turbidity, alternating with wind events (Regime II), sometimes leading to rapid increases in turbidity (Figure 6a,f). Settling dominates throughout the summer, with the turbidity generally following the exponential decline characteristic of particle-settling dominated systems [36]. However, the decline is interrupted by wind events, coinciding with small, short-lived increases in turbidity. In fall, Regimes I and II alternate, followed by a period of convective cooling that mixes turbid water into the epilimnion (Regime III).

4.1 Spring Turbidity

While all the numerical simulations started with an epilimnetic turbidity of 5.2 NTU on 22 May, by 20 June the modelled epilimnetic turbidities ranged from 1.8 NTU to 14 NTU (Figure 6f). To a remarkable degree, the turbidity at the end of spring (20 June) sets the turbidity for the duration of summer when particle settling dominated in all model runs (Figure 6f). Therefore, it is important to focus on the processes affecting epilimnetic turbidity from 22 May to 20 June (which for the sake of simplicity we will call "spring"). Four representative simulations, highlighted using coloured lines in Figure 6, are examined in detail. In the first case (the simulation driven by 2015 flow data) the bathymetric inflow factor $I_B < 1$ throughout spring (Figure 6e), primarily because the water level was high, resulting in low values of the ratio β/A_{pyc} (Figure 6d). In each of the subsequent cases (the simulations driven by the 2011, 2017 and 1999 flow data), I_B was successively higher and the relative importance of the bathymetric effect increased. As a consequence, the turbidity at the end of spring, Tu_1, increased as $\bar{I}_B$ increased (Figure 6f, Table 1), where we calculate $\bar{I}_B$ as the average value during spring, i.e., 22 May – 20 June.

4.1.1 Spring 2015 ($\bar{I}_B = 0.5$)

The 2015 model run is representative of simulations where $\bar{I}_B \ll 1$ during spring. During calm periods, the pycnocline rose due to net flow into the hypolimnion (Figure 7b,d,f), and turbidity declined due to particle settling (Figure 6f). During windy periods, the epilimnion tilted down toward the dam (Figure 7c,e,g), but winds were too weak to upwell significant quantities of turbid water into the epilimnion. Instead, turbidity at Station C2 continued to decline despite the windstorms (grey regions in Figures 6a, 7a). Overall, in the 2015 model

Table 1: Spring reservoir water level, volume, bathymetric inflow parameters, and turbidity in selected years.

Year	$z_{\mathrm{ws},0}$ (m)	V_0 (Mm^3)	$\bar{\beta}$ (−)	$\overline{\beta/A_{\mathrm{pyc}}}$ (km^{-2})	$\bar{Q}_{\mathrm{hyp}}$ (m^3 s^{-1})	$\bar{I}_B$ (−)	Tu_1 (NTU)
2015	636	399	0.23	0.008	131	0.5	1.8
2011	629	208	0.35	0.021	116	0.9	2.5
2017	619	71	0.40	0.039	96	1.8	8.9
1999	614	37	0.44	0.079	105	2.5	14

Notes:
[1]Reservoir water level, $z_{\mathrm{ws},0}$, and volume, V_0, at the start of the model run (22 May)
[2]Overbars denote time-averaged quantities over spring (22 May – 20 June)
[3]Turbidity Tu_1 at Station C2 at 1 m depth at the end of spring (20 June)
[4]Turbidity $Tu_0 = 5.2$ NTU for all model runs

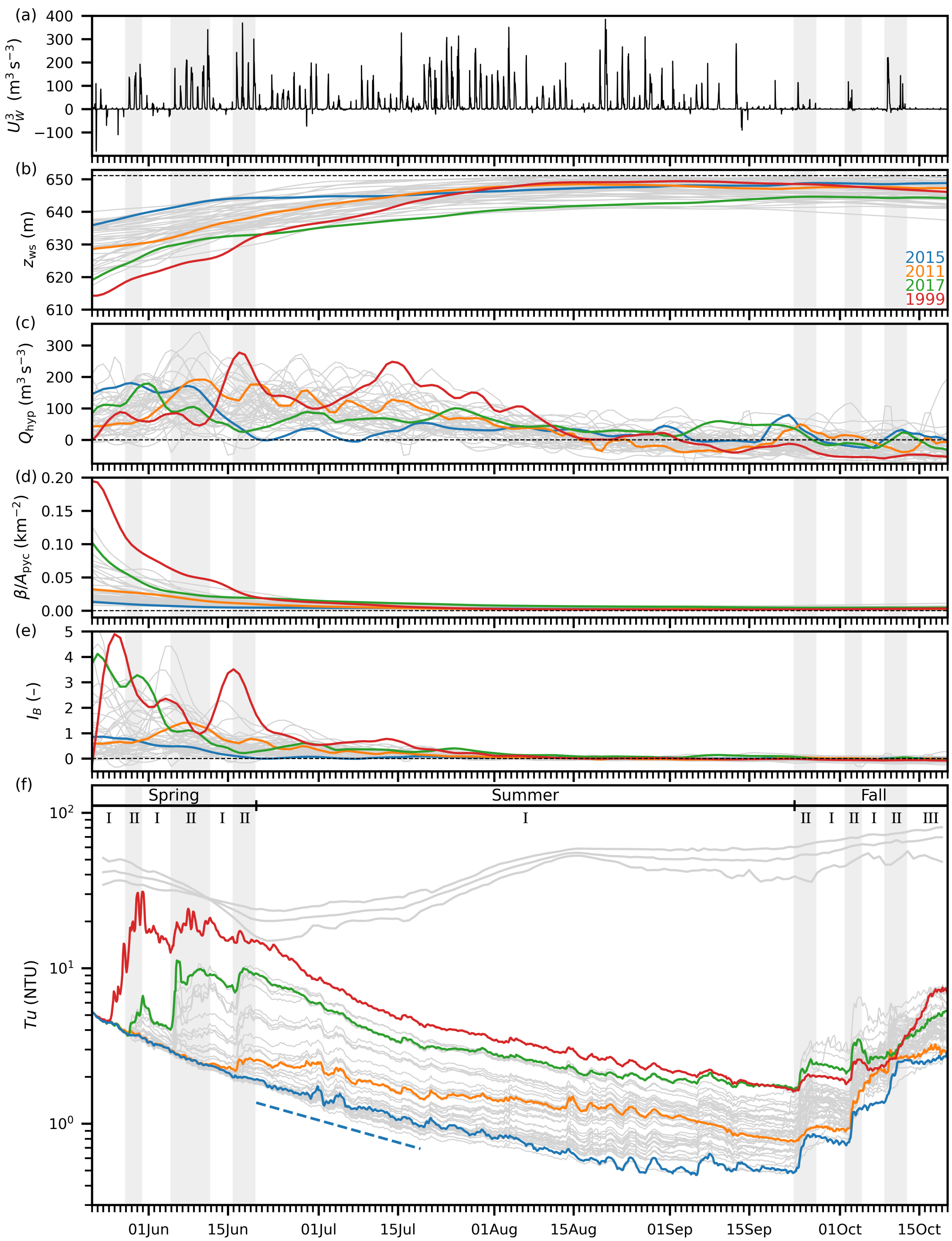

Figure 6: Time series of (a) observed along-axis wind speed cubed, U_W^3, and simulated (b) reservoir water level, z_{ws} (c) hypolimnetic flow, Q_{hyp} (d) bathymetric factor divided by the surface area of the pycnocline, β/A_{pyc} (e) bathymetric inflow parameter, I_B (f) turbidity at Station C2 at 1 m depth, Tu. In (a), positive wind speed is from the west toward the dam. In (b), the dashed line marks the elevation of full pool. In (b–f), the thin grey lines show the model results for all years 1965 – 2017, and the coloured lines show selected years. In (c), the blue dashed line shows Eq. (10) for $w_s = 0.2$ m d^{-1} and $h_{\mathrm{epi}} = 8.5$ m. In (f), the thick grey lines show the flow-weighted turbidity of the inflows (median, 5th and 95th percentile). Roman numerals mark Regimes described in the text.

run, the spring period saw a significant decline in turbidity, and, as a result, summer began with an initial turbidity far lower than for most other model runs (Figure 6f).

4.1.2 Spring 2011 ($\bar{I}_B = 0.9$)

The 2011 model run is representative of simulations where $\bar{I}_B \approx 1$ during spring. In these simulations, only the third windstorm led to increases in turbidity. These increases were less than the decreases due to particle settling; the combined effect was a net decline in turbidity during spring (Figures 6f, 7h–m).

4.1.3 Spring 2017 ($\bar{I}_B = 1.7$)

The 2017 model run is representative of simulations where $\bar{I}_B > 1$ during spring, and the epilimnetic turbidity at Station C2 increased during all three windstorms. Despite turbidity decreases due to particle settling during calm periods, there was a net increase in turbidity during spring. On 28 May, just before the first windstorm, the reservoir volume was only 11% of capacity (Figure 7n) and just one quarter of the reservoir volume as on the same day in 2015 (Figure 7b). At this time, the reservoir was only 15 km long with the upstream 7 km dominated by inflows and the epilimnion extending the remaining 8 km to the dam wall (Figure 7n). In the 2015 model run, by contrast, the reservoir just before the first windstorm was 35 km long with the upstream 5 km dominated by inflows and the epilimnion extending 30 km to the dam wall (Figure 7b). In the 2017 model run, during the first windstorm (28 – 30 May), turbidity at Station C2 nearly doubled (Figure 6f), and the wind pushed the surface water toward the dam, shortening and deepening the epilimnion (Figure 7o). As the epilimnion deformed under wind stress, turbid water was mixed into the epilimnion, with a small daily jump in turbidity following the diurnal wind (28 – 30 May, Figure 6a, f). This contrasts with 2015, when, over the same period, turbidity declined (Figure 6f).

From 30 May to 5 June, during a calm period, the wind subsided and the epilimnion returned to its undisturbed position (Figure 7p). Without wind stress to balance the pressure gradient set up by the previous windstorm, surface currents changed direction from downstream (toward the dam) to upstream. The region dominated by inflow retreated upstream at 3 $\mathrm{km\,d^{-1}}$, roughly consistent with the baroclinic wave speed within the epilimnion, $c \approx \frac{1}{2}\sqrt{g' h_{\mathrm{epi}}} = 4.5\ \mathrm{km\,d^{-1}}$. By 5 June, the turbidity at Station C2 had declined (Figure 6f), but it remained higher than the turbidity at the start of the model run, and higher than on the same date in the 2015 and 2011 model runs. For the remainder of spring, the turbidity responded in a similar manner, increasing during windy periods and decreasing during calm periods.

So far, increases in turbidity have resulted from two mechanisms. First, localized wind-driven deepening of the epilimnion mixed turbid, metalimnetic fluid into the surface waters. In this case, turbidity responded within hours of a wind impulse, often giving rise to jumps in turbidity (e.g. 5 June; Figure 6f). Second, surface wind-driven currents transported upwelled turbid water from the upstream portion of the reservoir toward the dam, driving an increase in turbidity at Station C2 (e.g. 7 – 10 June; Figure 6f). We now look at a third mechanism where increases in turbidity are triggered by inflow.

4.1.4 Spring 1999 ($\bar{I}_B = 2.6$)

At the beginning of the 1999 model run, on 22 May, the reservoir was drawn down to a depth of 13 m and a volume of 35 $\mathrm{Mm^3}$, just 3% of the reservoir volume at full pool and an order of magnitude smaller than the volume on the same date in 2015 (Table 1). The reservoir volume more than doubled by 25 May, and nearly all the reservoir upstream of Station C2

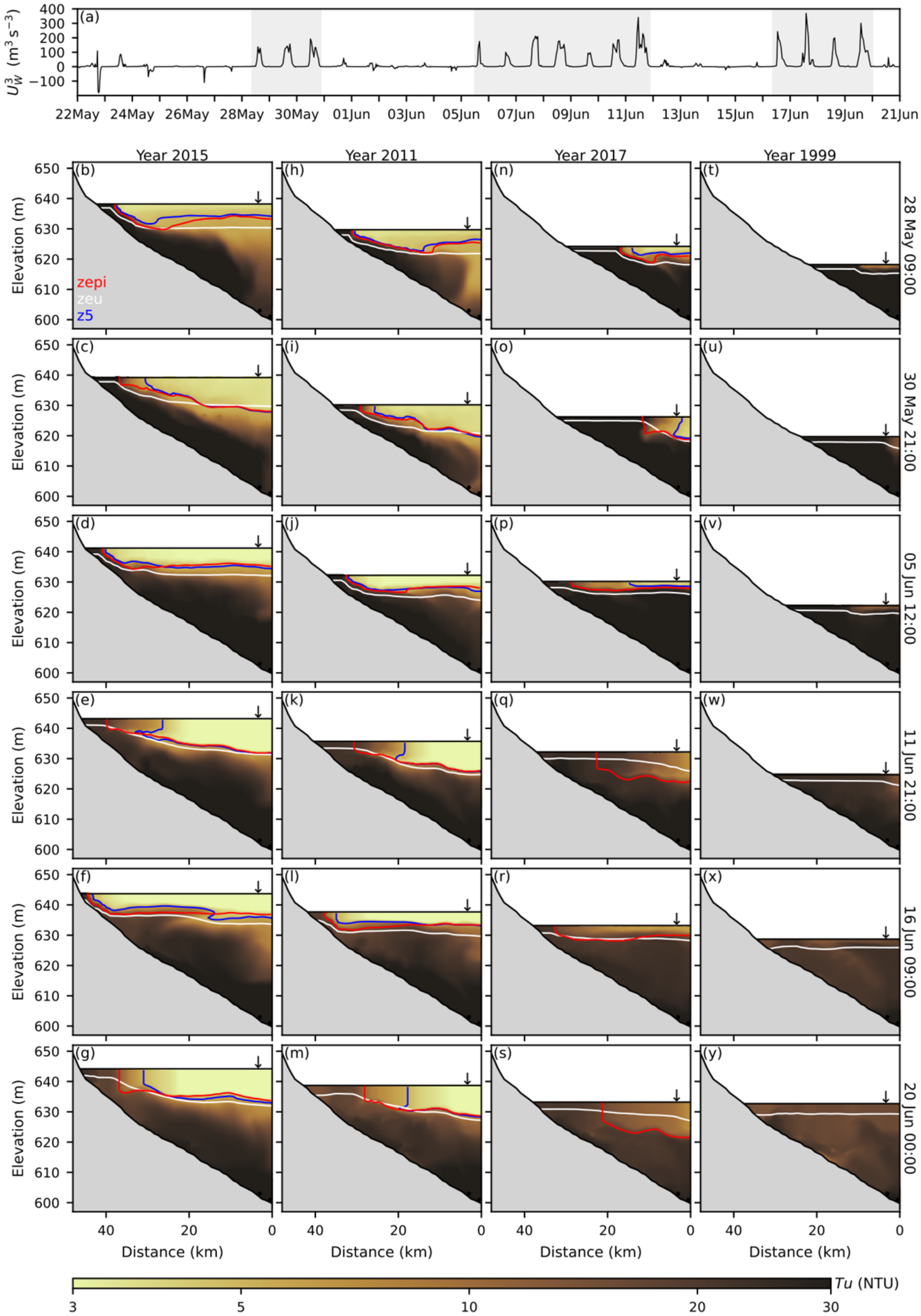

Figure 7: Modelled turbidity before and after each wind event in spring. (a) Observed along-axis wind speed cubed and (b–y) snapshots of modelled turbidity for the 2015, 2011, 2017 and 1999 model runs during the spring period (22 May – 20 June). The white line marks the euphotic depth. The red line (if present) marks the thermocline depth. The blue line (if present) and the water surface bound the region where turbidity is less than 5 NTU. In (b–y), the downward arrow marks Station C2. The shading in (a) indicates the wind events in spring. The snapshots in (b–y) were taken at the beginning and end of each wind event. The times are indicated on the right-hand side of each row of snapshots. Note the same wind forcing is used for all model runs shown, see Section 3.

was occupied by well-mixed inflow that had entered the reservoir since the beginning of the simulation; that is, well-mixed riverine conditions extended to Station C2. The rapid filling of the reservoir mixed turbid water into the epilimnion and turbidity nearly doubled on 25 May (Figure 6f). Note that conditions during this day were calm, indicating that the mixing event leading to the increase in turbidity was triggered by inflow instead of wind-driven mixing.

As the reservoir filled further, subsequent jumps in turbidity at Station C2 coincided with windstorms, following the pattern of the 2017 model run (Figure 6f). After the first windstorm (28 – 30 May), the turbidity at Station C2 in the 1999 model run increased to ~ 30 NTU, comparable to that of the inflow (Figure 6f).

4.1.5 Epilimnetic Turbidity at the End of Spring and the Bathymetric Inflow Parameter

The epilimnetic turbidity at the end of spring, Tu_1, is plotted against the average bathymetric inflow parameter during spring for each of the 46 simulations (Figure 8). Note that in most of the simulations, the turbidity declined over the spring ($Tu_1/Tu_0 < 1$, Figure 8, dotted line). In cases where $\bar{I}_B \ll 1$, Tu_1 is either equal to, or slightly above the value associated with particle

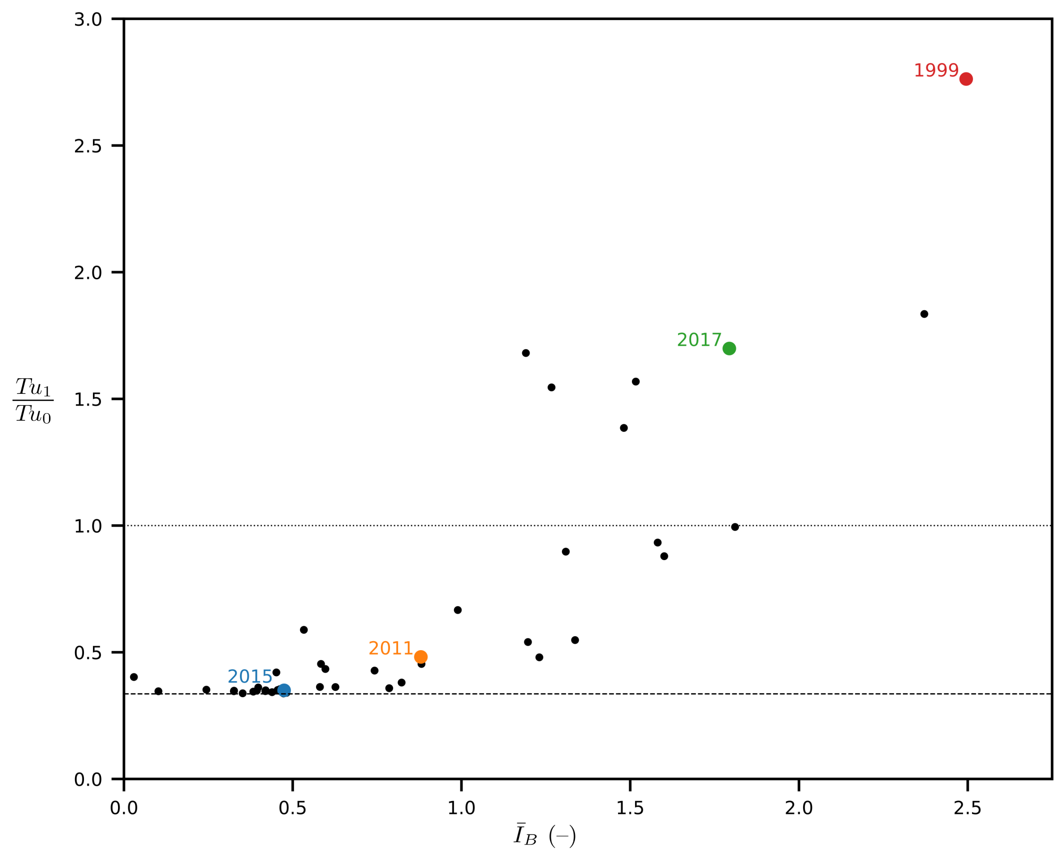

Figure 8: Relation between epilimnetic turbidity at Station C2 at 1 m depth at the beginning of summer, divided by the initial turbidity Tu_1/Tu_0, and the average bathymetric inflow parameter, $\bar{I}_B$ from the beginning of the model run to the beginning of summer (22 May – 20 June). The black dots show the model results for all years 1965 – 2017, and the coloured dots show selected years. The dashed line indicates a lower bound estimate of epilimnetic turbidity at the end of spring due to particle settling only (in the absence of the bathymetric effect) for $h_{\text{epi}} = 5.5$ m and $w_s = 0.2$ m d^{-1}, see Eq. (10). The dotted line indicates $Tu_1/Tu_0 = 1$.

settling (Figure 8, dashed line, calculated using (10) with $h_{\mathrm{epi}} = 5.5$ m and $w_s = 0.2\ \mathrm{m\,s^{-1}}$), indicating that particle settling was by far the dominant mechanism affecting epilimnetic turbidity during these simulations. By contrast, for larger $\bar{I}_B$, Tu_1 generally increases with increasing $\bar{I}_B$, providing clear evidence of the importance of the bathymetric effect.

4.2 Summer

In all 46 simulations, epilimnetic turbidity during summer was characterized by an approximately exponential decline, consistent with particle settling being the primary driver of turbidity variations and $I_B < 1$ (Figure 6e,f). Nevertheless, wind-driven seiching also played an important role that we now investigate.

During the first 30 days of summer (21 June – 20 July) in the 2015 model run, turbidity at Station C2 at 1 m depth declined with an e-folding time of $\tau_s \approx 48$ d (Figure 6f). During this period, the modelled (and observed) epilimnetic depth was ≈ 8.5 m, corresponding to an effective particle settling velocity of $w_s^{\mathrm{eff}} = 0.18\ \mathrm{m\,d^{-1}}$. This value is close to the settling velocity specified in the model, $w_s = 0.2\ \mathrm{m\,d^{-1}}$ (blue dashed line, Figure 6f), confirming that particle settling is a dominant driver of turbidity variations during summer, but indicating that there may have been mixing due to the shear associated with wind-driven thermocline oscillations (internal seiches). During the next 30 days (20 July – 19 August), winds were stronger — they imparted $\sim 70\%$ more energy to the water surface — and the effective settling velocity decreased further.

The thermocline oscillated with two dominant periods. First, basin-scale oscillations with a period of approximately four days are evident in the wave characteristics plots for each of our selected years (2015, 2011, 2017 and 1999), e.g. green lines in Figure 9e. For 21 June to 2 September, the Merian formula (8) gives the phase speed, $c_p \approx 19 \pm 2\ \mathrm{km\,d^{-1}}$ and the fundamental internal seiche period, $T_1 \approx 4.1 \pm 0.6$ d, consistent with the values of c_p and T_1 obtained from the wave characteristics (Figure 9). The second oscillatory period corresponds to the diurnal wind forcing, T_f. The prevailing wind blows down valley in the afternoon, resulting in a series of daily wind impulses. With each impulse, a depression of the thermocline was generated at the dam, which propagated upstream toward the plunge point (e.g. blue lines, Figure 9e). The upstream propagating wave then reflected off the inflow and traveled back downstream (e.g. red lines, Figure 9e). The inverse slope of the lines gives $c_p \approx 18\ \mathrm{km\,d^{-1}}$, consistent with our estimate using the Merian formula.

The two-dimensional spectra of the thermocline oscillations are shown in Figure 10. There are distinct peaks in the spectra at the period of $T_f = 1$ d and wavelength $\lambda = 18$ km, corresponding to the daily wind forcing. At the period of $T_1 \approx 4.1$ d, corresponding to the fundamental basin-scale seiche, there is a broader band in response to the changes in stratification and water level over the summer. Also shown are the lines corresponding to $c_p = 19\ \mathrm{km\,d^{-1}}$, as predicted using the Merian formula, and consistent with our estimates based on the plot of wave characteristics (Figure 9).

The response of the thermocline in the four selected model runs was similar (Figure 9); this is not surprising given that the wind forcing was the same for all model runs shown. However, there remain differences between the model runs due to changes in stratification and water level. There were also changes within a given year. For example, in early July of the 1999 model run, low L and high g' resulted in a shorter than average basin-scale seiche period (3.8 d, magenta lines), compared with late August 1999 when high L and low g' resulted in a longer seiche period (4.5 d, green lines), see Figure 9e. Internal waves, due to daily wind forcing and basin-scale internal seiches, modulate the epilimnetic turbidity at any given location (Figure 11d).

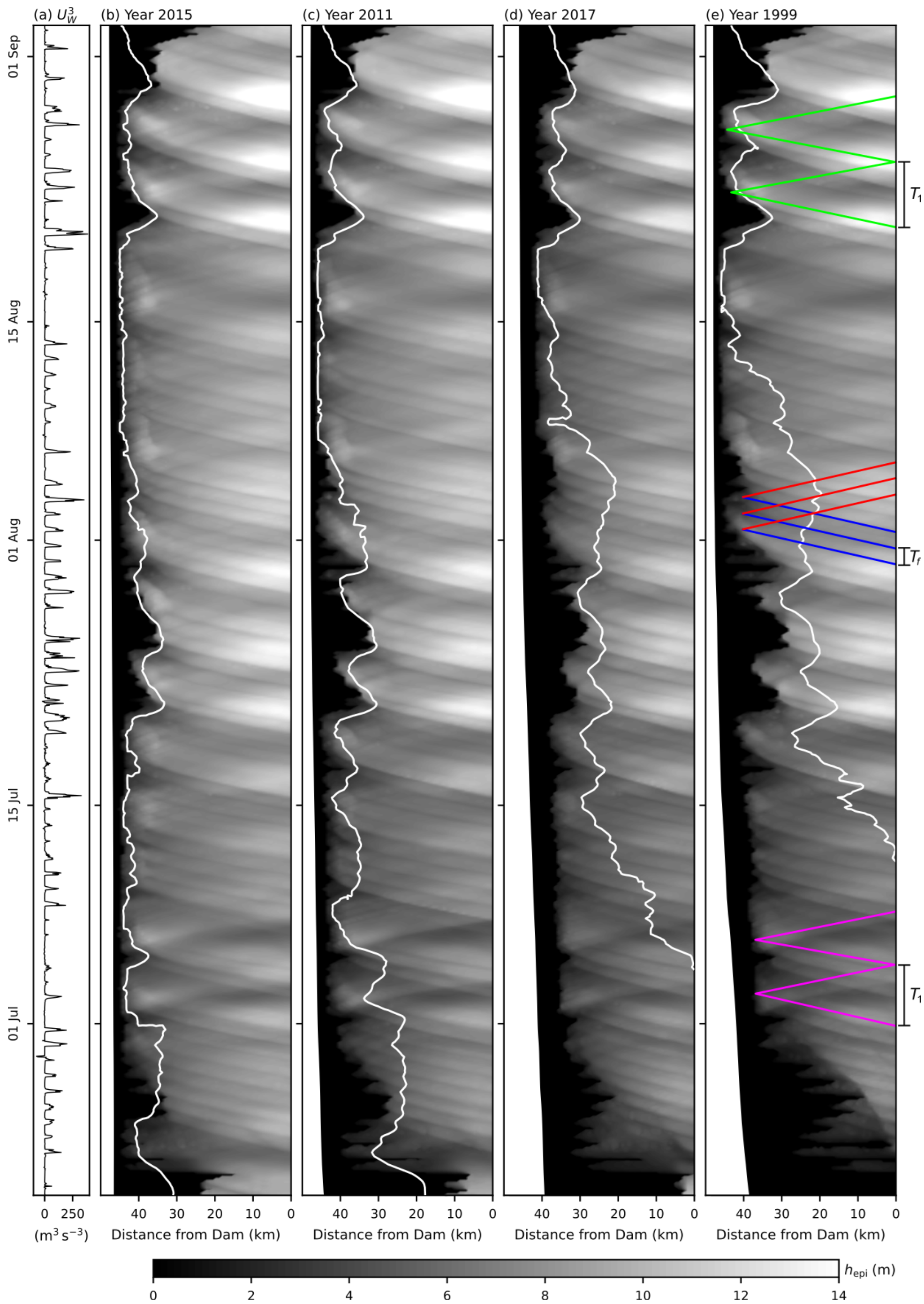

Figure 9: (a) Along-axis wind speed cubed observed in 2015; positive wind is from the west toward the dam. (b–e) Wave characteristics plots of the modelled thermocline depth for the 2015, 2011, 2017 and 1999 model runs. The shading represents the depth of the thermocline below the water surface. The dark bands represent waves of elevation (crests), while light bands represent waves of depression (troughs). The phase velocity is given by the inverse slope of these bands: a more vertical band indicates a slower-moving wave, and a more horizontal band indicates a faster-moving wave. The white line indicates the 5 NTU contour at the water surface; the region bounded by the contour and the dam has a surface turbidity <5 NTU. Recall that the meteorological forcing is the same for all model runs shown. In (e), the coloured lines trace representative oscillations of the thermocline at two dominant periods: basin-scale oscillations (T_1, green and magenta) and oscillations due to diurnal wind forcing (T_f, red and blue).

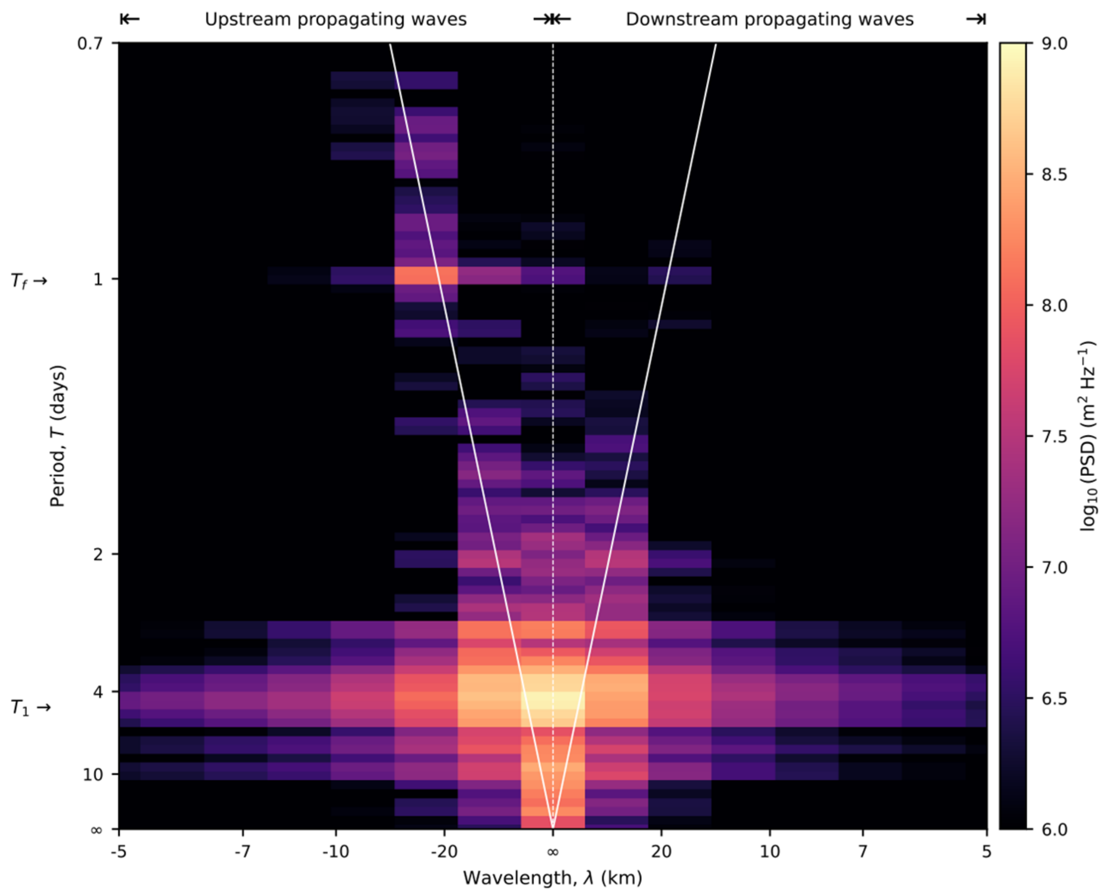

Figure 10: Power spectral density (PSD) obtained by the two-dimensional Fourier transform of the modelled wave characteristics shown in Figure 9b (the 2015 model run). Results for 2011, 2017, and 1999 are similar. The excited frequency band at 1 day corresponds to direct forcing by diurnal winds, T_f, and the broader band centered at 4.1 days corresponds to the fundamental internal seiche, T_1. Positive and negative wavelengths correspond to downstream and upstream propagating waves, respectively. The solid white lines correspond to the phase speed $c_p = 19$ km d^{-1} predicted using the Merian formula.

4.3 Fall

The bathymetric effect is based on the assumption that epilimnetic depth remains approximately constant; this is not the case in fall when the epilimnion generally deepens. So even though the bathymetric factor in fall is always below unity, increases in turbidity due to wind-driven mixing and penetrative convection occur. In fall, there were three windy periods followed by calm periods (Figure 6a). During the wind events the epilimnion deepened, and the epilimnetic turbidity increased due to the entrainment of higher turbidity water from the metalimnion. During the first calm period, the epilimnetic turbidity generally decreased as particle settling dominated. During the third calm period penetrative convection dominated and turbidity increased. Overall, during fall, epilimnetic turbidity increased substantially in all model runs (Figure 6f).

5 Discussion

Here we discuss the physical processes affecting epilimnetic turbidity in glacier-fed hydroelectric reservoirs and the impacts that these processes, reservoir operations, and hydrological conditions have on epilimnetic turbidity and water quality.

5.1 Physical Processes

5.1.1 The Bathymetric Effect

The primary motivation for the present study was to test the hypothesis that the bathymetric effect can be an important factor in determining epilimnetic turbidity in hydroelectric reservoirs, and in Carpenter Reservoir in particular. The bathymetric effect consists of two processes:

1. When the spring freshet plunges into the hypolimnion, the epilimnion is displaced upwards and thins as it spreads over a larger area, see Section 2.5.

2. The thinner epilimnion is then more susceptible to wind-driven upwelling, which entrains and mixes turbid water from the metalimnion into the less turbid epilimnion, see Section 2.6.

The increase in epilimnetic turbidity due to these processes competes with the reduction in epilimnetic turbidity due to particle settling.

The bathymetric inflow parameter, $I_B \equiv \frac{\beta Q_{\mathrm{hyp}}}{A_{\mathrm{pyc}} w_s}$, see Section 2.5, reflects the relative importance of the bathymetric effect with respect to particle settling. For the 46 scenarios modelled, in general the higher (lower) I_B during spring, the higher (lower) the epilimnetic turbidity at the end of spring (Figure 6 and Table 1). The Wedderburn number, $W = \frac{g' h_{\mathrm{epi}}^2}{u_*^2 L}$, see Section 2.6, reflects the susceptibility of a lake to wind-driven upwelling and mixing. Here we discuss how variations in I_B and W explain the temporal and spatial variations in epilimnetic turbidity in the 2017 model run.

The temporal variations of W and I_B in the 2017 model run are presented in Figure 11a,b. The Wedderburn number ranged from $O\left(10^{-1}\right)$ to $O\left(10\right)$ with the lowest values occurring during the three windstorms in spring (Figure 11a). At the start of the simulation $I_B \approx 4$; it then decreased to unity by the middle of June, and for the rest of the study $I_B < 1$ (Figure 11b). While I_B was influenced by variations in Q_{hyp}, the primary factor influencing I_B was β/A_{pyc}; as the reservoir filled during spring freshet, the bathymetric factor decreased and the pycnocline area increased (Figure 4b). As a consequence, fluctuations in turbidity along the length of the epilimnion were most dramatic during the windstorms of spring.

The temporal variations of turbidity at stations C2, C4 and C6 are presented in Figure 11c, and contours of turbidity as a function of distance from the dam and time in Figure 11d. The simulation started on 22 May in a period of relative calm ($W \gg 1$) that lasted until the first windstorm on 28 May. During this calm period, the epilimnetic thickness decreased from its initial value of 10 m to approximately 4 m (Figure 7n). The predicted variation in epilimnetic depth due to the bathymetric effect in the absence of wind is given by (8): $\mathrm{d}h_{\mathrm{epi}}/\mathrm{d}t = -\beta Q_{\mathrm{hyp}}/A_{\mathrm{pyc}}$, which for $Q_{\mathrm{hyp}} \approx 110\ \mathrm{m^3\,s^{-1}}$, and $\beta/A_{\mathrm{pyc}} \approx 8 \times 10^{-8}\ \mathrm{m^{-2}}$ (Figure 6c,d); gives $\mathrm{d}h_{\mathrm{epi}}/\mathrm{d}t \approx -0.8\ \mathrm{m\,d^{-1}}$, consistent with the simulated decrease in epilimnetic depth. During this period epilimnetic turbidity at C2 and C4 decreased approximately exponentially, due to particle settling, as we would expect. The behaviour at C6 will be explained below.

During the remainder of spring (29 May – 20 June) there were three windstorms during which $W < 1$ and $I_B > 1$ (Figure 11a,b). Consequently, the epilimnetic turbidity increased (Figure 11c,d), and the epilimnetic thickness increased (Figure 7n–s). During the periods

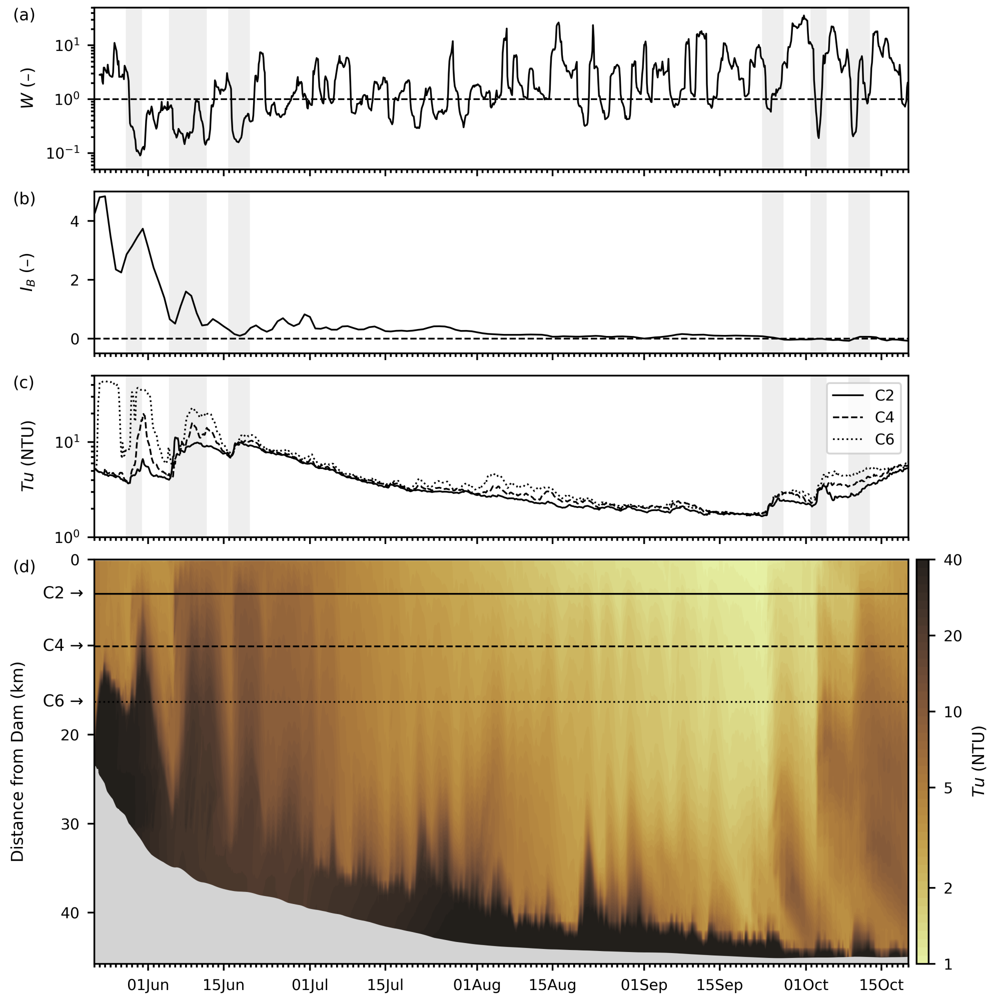

Figure 11: 2017 model run. Time series of (a) Wedderburn number W, (b) bathymetric inflow parameter I_B, (c) turbidity at 1 m depth at stations C2, C4 and C6, (d) turbidity at 1 m depth along the length of the reservoir (colormap, logarithmic scale). In (d), the grey area represents the draw-down zone (the area upstream of the reservoir that is dry when the water level is low).

of calm between the windstorms, the turbidity decreased due to particle settling and the epilimnion thinned due to hypolimnetic inflow.

Throughout the summer $I_B < 1$, and $W > 0.5$, so in general particle settling dominated, and epilimnetic turbidity decreased approximately exponentially (Figure 6f). While some weak upwelling events occurred, they did not last long enough for the upwelled water to have a significant impact at stations C2, C4 and C6 (Figure 11c,d).

While there were increases in turbidity during wind events in fall, these cannot be attributed to the bathymetric effect since $I_B \approx 0$ throughout the latter part of summer and during fall. There are two factors to consider. First, the weak stratification in fall makes the epilimnion more sensitive to a given wind event, since the low g' results in low values of W. Furthermore, thermal convection becomes a factor throughout fall, and in particular towards the end of the simulation when turbidity continued to increase even in the absence of wind (Figures 6f, 11c,d).

5.1.2 Upwelling and Longitudinal Variations in Turbidity

For $W < O(1)$ metalimnetic fluid was upwelled as depicted in Figure 5. In the contours of temperature for 18 June 2015, the metalimnion extends from approximately 10 to 18 °C (Figure 5b). The metalimnion is upwelled with the 14 to 18 °C isotherms reaching the surface. As a result, turbidity from the metalimnion, with isolines ranging from 2 to 10 NTU, reaches the surface (Figure 5c). Recall that wind was channelized along the river valley, and note here how upwelling follows the thalweg, irrespective of the slight curve to the reservoir (Figure 5b,c). Once upwelled fluid reached the surface it was advected downstream by wind-driven surface currents, often resulting in more turbid water near the top of the epilimnion than deeper in the epilimnion, as can be seen in Figure 7e,g,k,m,o. Mixing was then dominated by longitudinal dispersion of horizontal turbidity variations created by upwelling. Almost invariably, turbidity at a given depth in the epilimnion decreased in the downwind direction, as is evident in Figure 11c,d.

5.1.3 Dynamic Effects of Inflows

An exception to the downwind longitudinal turbidity gradient occurred in the 2017 model run at the start of the second windstorm (5 June) when the turbidity at C2 jumped suddenly and remained higher than at C4 and C6 for a duration of approximately one day (Figure 11c,d). At this time the simulation reveals a disturbance associated with inflow that reflected off the dam and travelled upstream, resulting in a local thinning of the epilimnion. The shear between the wind-driven surface current and this disturbance shed turbid water from the top of the disturbance, thereby increasing turbidity at C2. As the disturbance moved upstream, it weakened and did not affect epilimnetic turbidity at stations upstream of C2, see Figure 11c,d. Note also that the turbidity was elevated at C6 even during the first two periods of relative calm (23 – 27 May, 31 May – 3 June). This occurred because the location where the dense inflow plunged below the water surface (plunge point) extended downstream of C6, see Figure 7n and Figure 11d, due to low water level and high inflow early in the simulation, see Figure 6b,c. As the reservoir filled, the plunge point moved further upstream, and the turbidity at C6 was less affected by the plunging inflow.

The impact of inflows was most dramatic in the 1999 model run. Initially, the volume of water in the reservoir was very small and the inflow overwhelmed the water in the reservoir, see Figure 7t–y. This scenario is outside the scope of the present study, which focuses on the bathymetric effect. Even though the 1999 scenario was initiated with a 10 m deep epilimnion, it was quickly destroyed by the inflow (Figure 7t).

5.1.4 Seiching

In addition to the processes described above, internal seiches — at both the fundamental seiche period and diurnally — cause fluctuations in epilimnetic turbidity. For example, fluctuations in the position of the 5 NTU contour at the surface of the reservoir often coincide with these seiches, as is graphically demonstrated in Figure 9.

5.2 Implications for Epilimnetic Turbidity and Water Quality

Elevated turbidity in the epilimnia of lakes and reservoirs in glaciated catchments often presents ecological concerns. A turbidity of 5 NTU has been suggested as the threshold for the beginning of light limitation for primary production in glacial lakes [8], and the threshold above which glacial flour can interfere with filter-feeding in cladocerans [19], a key food source for kokanee. The turbidity of the inflow to Carpenter Reservoir in spring and summer

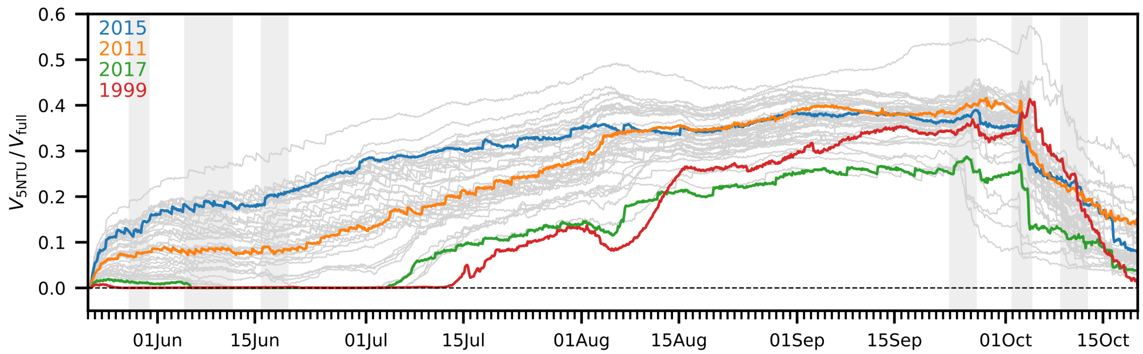

Figure 12: Simulated volume of the reservoir with a turbidity less than 5 NTU, $V_{5\mathrm{NTU}}$, divided by the reservoir volume at full pool, V_{full}, (651.08 m asl, 1.0×10^9 m^3). The thin grey lines show the model results for all years 1965 – 2017, and the coloured lines show selected years.

is typically 20 – 60 NTU (Figure 6f). Concerns that elevated turbidity could decrease fisheries productivity within Carpenter Reservoir [3] were alleviated by field measurements of epilimnetic turbidity in 2015 that were invariably below 5 NTU, except at the upstream end of the reservoir at the beginning of summer [29]. However, 2015 may have been unusual in that the water levels were high during spring and the bathymetric effect low compared to other years.

A useful metric to compare 2015 with other years is the volume of water with a turbidity of less than 5 NTU, $V_{5\mathrm{NTU}}$, see Figure 12. Note that the turbidity of the inflow into Carpenter Reservoir was always greater than 5 NTU (Figure 6f), meaning that under well-mixed conditions $V_{5\mathrm{NTU}}$ would equal zero. However, thermal stratification and particle settling result in a much lower turbidity in the epilimnion than at depth. In all scenarios, the decline in summer epilimnetic turbidity led to an increase in $V_{5\mathrm{NTU}}$, reaching a maximum in late summer and early fall (Figure 12), followed by a rapid decline in fall as the surface mixed layer deepened. For scenarios with low water levels during spring (1999, 2017 and six others), $V_{5\mathrm{NTU}}$ remained equal to zero well into the summer, potentially truncating the biologically productive season. In fact, in 1999, $V_{5\mathrm{NTU}} = 0$ until 13 July. A similar criterion could be applied to systems where other water quality parameters are a concern, for example, contaminants [17] or nutrients [31].

In Carpenter Reservoir, as in many glacier-fed water bodies, turbidity controls the volume of the euphotic zone [30]. As described above, a remarkable contrast between epilimnetic and hypolimnetic turbidity developed due to stratification and the settling of particles. By late summer, epilimnetic turbidity declined to 0.5 – 2 NTU (Figure 6f), whereas hypolimnetic turbidity remained elevated, ranging from 5 – 30 NTU (e.g. Figure 2h). To see the implications of this contrast, consider that the range of epilimnetic turbidity from 0.5 – 2 NTU corresponds to a range of euphotic depth from 13 – 20 m, see Figure 3 in Robb et al. [29]. However, the epilimnion was shallower than this, typically ≈ 8 m, and the presence of more turbid water below the epilimnion means that light passing through the epilimnion is rapidly attenuated just below the epilimnion [28, Equation 4.3]. As a result, the summer euphotic zone generally ended close to the top of the turbid hypolimnion and the euphotic depth followed the oscillations of the thermocline in response to wind (Figure 2h). Despite the high turbidity of inflow to the reservoir, the entire epilimnion was within the euphotic zone during almost all of summer.

In 2017, the hydroelectric utility lowered water levels in Carpenter Reservoir to accommodate high outflows from La Joie Dam (Figure 1a). These outflows were required to reduce the water level in Downton Reservoir and the seismic risk in the ageing La Joie Dam. The model results suggest that drawdown in spring enhanced the bathymetric effect (Figure 6e) and contributed to higher turbidity in the epilimnion in 2017 (Figures 6f, 7n–s). The water level regime in subsequent years, 2018 – 2024, was similar to that in 2017 and will likely be representative of future conditions until anticipated repairs are completed.

6 Summary

We used a hydrodynamic model in conjunction with 46 years of hydrological data to examine the temporal and spatial variation of epilimnetic turbidity in Carpenter Reservoir. The simulated fate of epilimnetic turbidity in Carpenter Reservoir highlights the consequences of the main feature of reservoirs, that the volume is subject to dramatic variation. For example, in temperate latitudes, reservoirs are typically drawn down by early spring to allow for storage of freshet inflow. In the present study all inflows were dense and plunged into the hypolimnion, and all outflows were from the hypolimnion, both of which are by no means uncommon in reservoirs. The absence of direct inflow to the epilimnion resulted in the isolation of the epilimnion and allowed for clearing of the epilimnion by particle settling during summer. With net inflow to the hypolimnion, the epilimnion was displaced upwards and thinned as it spread over an increasing area. The epilimnion was then more vulnerable to wind-driven upwelling and this bathymetric effect provided an indirect path for the transport of turbid water into the epilimnion.

We introduce a bathymetric inflow parameter, I_B, giving the balance between particle settling from the epilimnion and transport of turbid water into the epilimnion. When $\bar{I}_B < 1$ particle settling dominated, and when $\bar{I}_B > 1$ the turbidity at the end of spring increased with increasing $\bar{I}_B$ (Figure 8). As a result, the turbidity of the epilimnion of Carpenter Reservoir during summer varied by an order of magnitude between model years, depending on reservoir operations and hydrological conditions, particularly in spring. Note that at low enough water level, rapid increases in epilimnetic turbidity were driven by flow alone (1999, Figure 7). In all years, the turbid water that upwelled into the epilimnion at the upstream end was dispersed, giving rise to large gradients in surface turbidity along the length of the reservoir (Figure 11), as also observed in satellite images [28, Appendix B]. In addition, internal waves (Figures 9, 10) resulted in variation of the epilimnetic turbidity at any given location on multiple timescales (Figures 7, 11). Despite highly turbid inflows to the reservoir, the entire epilimnion was within the euphotic zone throughout summer in most simulations.

By introducing a framework that incorporates the bathymetric inflow parameter and the Wedderburn number, this study provides the foundation for understanding more complex configurations in which one or more of the above conditions are relaxed. Our results are applicable to a range of natural and constructed water bodies where the fate of dense inflows has important impacts on water quality. They will also inform water use planning for Carpenter Reservoir, which aims to balance a suite of reservoir functions including hydropower generation, aquatic ecosystem services, and cultural significance [3]. Potential future research includes examining the effect of warmer inflows into Carpenter Reservoir due to glacier loss [4] and investigating the effect of releases from Carpenter Reservoir on turbidity in the downstream Seton Lake [2].

Acknowledgements

We are grateful to St'át'imc Nation for allowing us to conduct fieldwork within their traditional territory. Funding and support were provided by BC Hydro, Limnotek Research and Development Inc., and St'át'imc Eco-Resources (SER) Ltd. Funding was also provided by the Natural Sciences and Engineering Research Council (NSERC) of Canada through the CRD, CGS and USRA programs. We thank Bonnie Adolf, Gilda Davis, and Jude Manahan of SER who managed the study as part of a larger water use planning project. Special thanks goes to Chris Perrin of Limnotek Research for the opportunity to collaborate on this project and for many discussions on all parts of this work. Access to BC Hydro field facilities was provided by Dorian Turner. Field support was provided by crews servicing concurrent projects in the Bridge River system: support included Allison Hebert and Shannon Harris of BC Ministry of Environment and Climate Change Strategy; Dani Ramos and Annika Putt of Instream Fisheries Research Ltd.; and Tyler Creasey and Jessica Hopkins of SER. Marc Laynes and Jeff Sneep are thanked for boat and field support. We are grateful to Shauna Bennett for data management. Odin Scholz (Split Rock Environmental Ltd.) and Brad Oleman (BC Ministry of Forests Lands and Natural Resource Operations) are thanked for support on access to meteorological data from the Five Mile Forest Service weather station. We also thank Thea Rodgers, Melanie Mewhort and Adjoa Quainoo, who assisted with instrument service and data analysis and whose salaries were subsidized by the UBC Work Learn program. Finally, we thank the anonymous reviewers for their helpful comments.

Author Contributions

DMR and RP conceived the numerical experiments. RP designed the observational study. DMR and RP contributed to field data collection. DMR conducted the data analysis and numerical modelling. DMR wrote the manuscript with contributions from RP and GAL. All authors approved the final submitted manuscript.

References

[1] K. Ashley, L. C. Thompson, D. C. Lasenby, L. McEachern, K. E. Smokorowski, and D. Sebastian. Restoration of an Interior Lake Ecosystem: the Kootenay Lake Fertilization Experiment. *Water Qual. Res. J. Can.*, 32(2):295–324, 1997. doi: 10.2166/wqrj.1997.021.

[2] C. Barouillet, B. F. Cumming, K. R. Laird, C. J. Perrin, and D. T. Selbie. Influence of glacial flour on the primary and secondary production of Sockeye Salmon nursery lakes: a comparative modern and paleolimnological study. *Can. J. Fish. Aquat. Sci.*, 76: 2303–2314, 2019. doi: 10.1139/cjfas-2018-0372.

[3] BC Hydro. Bridge-Seton water use plan monitoring program terms of reference. BRGMON-10. Technical report, 2014.

[4] L. A. Bird, A. N. Moyer, R. D. Moore, and M. Koppes. Hydrology and thermal regime of an ice-contact proglacial lake: implications for stream temperature and lake evaporation. *Hydrol. Process.*, 36:e14566, 2022. doi: 10.1002/hyp.14566.

[5] D. Bouffard and L. Boegman. Basin-scale internal waves. In L. Bengtsson, R. W. Herschy, and R. W. Fairbridge, editors, *Encyclopedia of Lakes and Reservoirs*, pages 102–107. Springer Netherlands, 2012. doi: 10.1007/978-1-4020-4410-6_240.

[6] T. M. Cole and S. A. Wells. CE-QUAL-W2: A two-dimensional, laterally averaged, hydrodynamic and water quality model, version 3.72. Technical report, Department of Civil and Environmental Engineering, Portland State University, Portland, Oregon, 2015. URL https://www.ce.pdx.edu/w2/.

[7] J. A. Downing, Y. T. Prairie, J. J. Cole, C. M. Duarte, L. J. Tranvik, R. G. Striegl, W. H. McDowell, P. Kortelainen, N. F. Caraco, J. M. Melack, and J. J. Middelburg.

The global abundance and size distribution of lakes, ponds, and impoundments. *Limnol. Oceanogr.*, 51(5):2388–2397, 2006. doi: 10.4319/lo.2006.51.5.2388.

[8] J. A. Edmundson and J. P. Koenings. The Effects of Glacial Silt On Primary Production, Through Altered Light Regimes and Phosphorus Levels, No. 68. Technical report, 1986.

[9] D. Finger, M. Schmid, and A. Wüest. Effects of upstream hydropower operation on riverine particle transport and turbidity in downstream lakes. *Water Resour. Res.*, 42 (8):W08429, 2006. doi: 10.1029/2005wr004751.

[10] H. B. Fischer and R. D. Smith. Observations of transport to surface waters from a plunging inflow to Lake Mead. *Limnol. Oceanogr.*, 28(2):258–272, 1983. doi: 10.4319/lo.1983.28.2.0258.

[11] G. Friedl and A. Wüest. Disrupting biogeochemical cycles - Consequences of damming. *Aquat. Sci.*, 64(1):55–65, 2002. doi: 10.1007/s00027-002-8054-0.

[12] R. K. Gelda, A. T. King, S. W. Effler, S. A. Schweitzer, and E. A. Cowen. Testing and application of a two-dimensional hydrothermal/transport model for a long, deep, and narrow lake with moderate Burger number. *Inland Waters*, 5(4):387–402, 2015. doi: 10.5268/iw-5.4.804.

[13] G. Grill, B. Lehner, A. E. Lumsdon, G. K. MacDonald, C. Zarfl, and C. R. Liermann. An index-based framework for assessing patterns and trends in river fragmentation and flow regulation by global dams at multiple scales. *Environ. Res. Lett.*, 10(1):015001, 2015. doi: 10.1088/1748-9326/10/1/015001.

[14] S. M. Hirst. Impacts of the operation of existing hydroelectric developments on fishery resources in British Columbia. Inland fisheries. Can. Manuscr. Rep. Fish. Aquat. Sci. 2093. Technical report, 1991.

[15] L. Jaun, D. Finger, M. Zeh, M. Schurter, and A. Wüest. Effects of upstream hydropower operation and oligotrophication on the light regime of a turbid peri-alpine lake. *Aquat. Sci.*, 69(2):212–226, 2007. doi: 10.1007/s00027-007-0876-3.

[16] M. Jönsson, L. Ranåker, A. Nicolle, P. Ljungberg, T. Fagerberg, S. Hylander, T. Jephson, K. Lebret, J. Einem, L. A. Hansson, P. A. Nilsson, E. Balseiro, and B. Modenutti. Glacial clay affects foraging performance in a Patagonian fish and cladoceran. *Hydrobiologia*, 663 (1):101–108, 2011. doi: 10.1007/s10750-010-0557-4.

[17] K. Knauer, H. M. Nepf, and H. F. Hemond. The production of chemical heterogeneity in upper mystic lake. *Limnology and Oceanography*, 45(7):1647–1654, 2000.

[18] U. G. Kobler, A. Wüest, and M. Schmid. Effects of Lake–Reservoir Pumped-Storage Operations on Temperature and Water Quality. *Sustainability*, 10(6):1968, 2018. doi: 10.3390/su10061968.

[19] J. P. Koenings, R. D. Burkett, and J. M. Edmundson. The Exclusion of Limnetic Cladocera from Turbid Glacier Meltwater Lakes. *Ecology*, 71(1):57–67, 1990. doi: 10.2307/1940247.

[20] T. Maavara, Q. Chen, K. Meter, L. E. Brown, J. Zhang, J. Ni, and C. Zarfl. River dam impacts on biogeochemical cycling. *Nat. Rev. Earth Environ.*, 1:103–116, 2020. doi: 10.1038/s43017-019-0019-0.

[21] A. Matzinger, R. Pieters, K. I. Ashley, G. A. Lawrence, and A. Wüest. Effects of impoundment on nutrient availability and productivity in lakes. *Limnol. Oceanogr.*, 52(6): 2629–2640, 2007. doi: 10.4319/lo.2007.52.6.2629.

[22] S. G. Monismith. An experimental study of the upwelling response of stratified reservoirs to surface shear stress. *Journal of Fluid Mechanics*, 171(-1):407–439, 1986. doi: 10.1017/s0022112086001507.

[23] C. H. Mortimer. Water movements in lakes during summer stratification; evidence from the distribution of temperature in windermere. *Philosophical Transactions of the Royal Society of London. Series B, Biological Sciences*, 236(635):355–398, 1952.

[24] R. Pieters and G. A. Lawrence. Plunging inflows and the summer photic zone in reservoirs. *Water Qual. Res. J. Can.*, 47(3-4):268–275, 2012. doi: 10.2166/wqrjc.2012.143.

[25] N. L. Poff and J. C. Schmidt. How dams can go with the flow. *Science*, 353(6304): 1099–1100, 2016. doi: 10.1126/science.aah4926.

[26] REN21. Renewables 2021 Global Status Report. Technical report, REN21 Secretariat, Paris, France, 2021.

[27] C. S. Reynolds. *The ecology of freshwater phytoplankton*. Cambridge University Press, Cambridge, 1984.

[28] D. M. Robb. *Physical processes affecting epilimnetic turbidity in a glacier-fed hydroelectric reservoir*. PhD thesis, University of British Columbia, 2023. URL `http://hdl.handle.net/2429/83818`.

[29] D. M. Robb, R. Pieters, and G. A. Lawrence. Fate of turbid glacial inflows in a hydroelectric reservoir. *Environ. Fluid Mech.*, 21:1201–1225, 2021. doi: 10.1007/s10652-021-09815-4.

[30] K. C. Rose, D. P. Hamilton, C. E. Williamson, C. G. McBride, J. M. Fischer, M. H. Olson, J. E. Saros, M. G. Allan, and N. Cabrol. Light attenuation characteristics of glacially-fed lakes. *J. Geophys. Res. Biogeo.*, 119(7):1446–1457, 2014. doi: 10.1002/2014jg002674.

[31] F. J. Rueda, W. E. Fleenor, and I. Vicente. Pathways of river nutrients towards the euphotic zone in a deep-reservoir of small size: Uncertainty analysis. *Ecol. Model.*, 202 (3-4):345–361, 2007. doi: 10.1016/j.ecolmodel.2006.11.006.

[32] K. E. H. Slemmons, J. E. Saros, and K. Simon. The influence of glacial meltwater on alpine aquatic ecosystems: a review. *Environ. Sci. Proc. Imp.*, 15(10):1794–1806, 2013. doi: 10.1039/c3em00243h.

[33] I. R. Smith. A simple theory of algal deposition. *Freshwater Biol.*, 12(5):445–449, 1982. doi: 10.1111/j.1365-2427.1982.tb00639.x.

[34] R. Sommaruga. When glaciers and ice sheets melt: consequences for planktonic organisms. *J. Plankton Res.*, 37(3):509–518, 2015. doi: 10.1093/plankt/fbv027.

[35] A. B. Sullivan, S. A. Rounds, S. Sobieszczyk, and H. M. Bragg. Modeling hydrodynamics, water temperature, and suspended sediment in Detroit Lake, Oregon. Technical report, U. S. Geological Survey, 2007.

[36] E. W. Tedford, G. Halferdahl, R. Pieters, and G. A. Lawrence. Temporal variations in turbidity in an oil sands pit lake. *Environ. Fluid Mech.*, 19:457–473, 2019. doi: 10.1007/s10652-018-9632-6.

[37] R. O. Thompson and J. Imberger. Response of a numerical model of a stratified lake to wind stress. In *2nd IAHR Symposium on Stratified Flows*, pages 562–570, Trondheim, Norway, 1980.

[38] C. J. Vörösmarty, M. Meybeck, B. Fekete, K. Sharma, P. Green, and J. P. M. Syvitski. Anthropogenic sediment retention: major global impact from registered river impoundments. *Glob. Planet. Change*, 39(1-2):169–190, 2003. doi: 10.1016/s0921-8181(03)00023-7.

[39] C. J. Vörösmarty, P. B. McIntyre, M. O. Gessner, D. Dudgeon, A. Prusevich, P. Green, S. Glidden, S. E. Bunn, C. A. Sullivan, C. R. Liermann, and P. M. Davies. Global threats to human water security and river biodiversity. *Nature*, 467(7315):555–561, 2010. doi: 10.1038/nature09440.

[40] S. Yoshikawa, J. Cho, H. G. Yamada, N. Hanasaki, and S. Kanae. An assessment of global net irrigation water requirements from various water supply sources to sustain irrigation: rivers and reservoirs (1960–2050). *Hydrol. Earth Syst. Sci.*, 18(10):4289–4310, 2014. doi: 10.5194/hess-18-4289-2014.